ELSEVIER

3D printed photocatalytic feed spacers functionalized with β-FeOOH nanorods inducing pollutant degradation and membrane cleaning capabilities in water treatment

Nurshaun Sreedhar, Mahendra Kumar, Samar Al Jitan, Navya Thomas [1], Giovanni Palmisano, Hassan A. Arafat *

Center for Membrane and Advanced Water Technology, Khalifa University of Science and Technology, Abu Dhabi, United Arab Emirates

A B S T R A C T

A novel 3D printed photocatalytic feed spacer was developed for use in membrane-based water and wastewater filtration systems. The spacer fulfilled two new functions; degradation of membrane-permeating pollutants in the feed and membrane cleaning, in addition to its basic role as membrane support. The spacer, designed based on a triply periodic minimal surface architecture, was coated with polydopamine-polyethyleneimine, on which a photocatalytic layer of β-FeOOH nanorods was mineralized. The photocatalytic performance of the spacer was demonstrated through the degradation of methylene blue and 4-nitrophenol, both in batch and crossflow ultrafiltration (UF) modes. The spacer also exhibited the ability to clean the membrane surface of three organic foulants (humic acid (HA), sodium alginate (SA) and bovine serum albumin (BSA)), with a flux recovery ratio of 92 %, 60 %, and 54 % achieved for SA, HA, and BSA, respectively. This enables a shift to spacer-centered photocatalytic membrane system approach in water and wastewater treatment.

1. Introduction

A growing list of water pollutants, including pharmaceuticals, organics, inorganics and heavy metals, are continuously released into surface and groundwater bodies [1,2]. In order to meet increasingly stringent regulations regarding these pollutants' concentrations in potable water, new water treatment technologies are constantly developed. Of these, advanced oxidation processes (AOP) are among the most viable options, due to their ability to generate simple end products such as H_2O and CO_2, and the ability to treat dissolved organic compounds in wastewater [2]. Various AOP, such as ozonation, Fenton process, photocatalysis, and electrochemical oxidation, have been extensively studied for their potential use in the degradation of harmful chemicals in water [3,4]. Photocatalysis in membrane systems (also referred to as photocatalytic membrane reactor, PMR) can be carried out in two ways: (i) the catalyst is suspended in the feed as slurry, or (ii) the catalyst is immobilized on the membrane surface. Both designs have exhibited merits and disadvantages [5,6]. Suspended photocatalysts show high reactivity, due to a greater surface area exposure. However, they require

downstream catalyst separation and recovery from the feed. On the other hand, photocatalytic membranes have the catalysts attached to their surface, in a combined photocatalysis/filtration process [5,7,8].

Many photocatalytic membranes were developed in recent years [9]. These utilize a range of catalytic surface additives, such as silver decorated titanium dioxide (TiO_2) (Ag-TiO_2) [10], graphene oxide (GO)/TiO_2 [11], graphitic carbon nitride/TiO_2 (mpg-C_3N_4-TiO_2) nanocomposite [12] and GO and triethanolamine (TEOA) linked titanate nanowires (TNWs) (GO-TEOA-TNWs) [13], to name some examples. Nitrogen-doped TiO_2 (N-TiO_2) which can operate in visible light was deposited on membranes using atomic layer deposition (ALD) for dye removal [14] as well as foulant degradation [15]. Iron oxyhydroxides (α-FeOOH and β-FeOOH) are also considered promising photocatalysts [16]. FeOOH nanoparticles were studied as a standalone photocatalyst [17] or combined with TiO_2 [18] or gC_3N_4 [19,20]. Mussel-inspired chemistry has been gaining significant attention in surface modification of the membranes through the formation of an even thin-layer of self-polymerizing dopamine that can be further modified in a variety of ways [21]. Recently, Lv et al. [22] developed an interesting concept for a

photocatalytic nanofiltration membrane with self-cleaning capability, using a facile biomimetic mineralization strategy. A polydopamine (PDA)/polyethyleneamine (PEI) thin layer was first deposited on the membrane surface, via mussel inspired co-deposition, and cross-linked with the porous membrane. A mineralization process was then implemented to generate the β-FeOOH nanorods on the surface of PDA/PEI layer supported membranes. The resulting composite membranes exhibited efficient photocatalytic activity for dyes degradation by the photo-Fenton reaction in the presence of hydrogen peroxide [22]. Similarly, Chen et al. fabricated a PVDF-g-PAA@FeOOH membrane where a catalytic β-FeOOH layer was formed via mineralization using $FeCl_3$ solution under acidic medium and used for the in degradation of e dyes and foulants in the presence of H_2O_2 by visible light photo-Fenton reaction [23].

In flat-sheet and spiral-wound module (SWM) system configurations, feed spacers perform the dual role of providing mechanical support to the membrane as well as enhancing the mass transfer through increased fluid turbulence [24]. In recent years, a new research area of chemical spacer modification has emerged, with the aim of inducing new properties of feed spacers, allowing them to perform additional roles besides their two key functions. These include anti-bacterial capabilities [25], resistance to foulant adhesion on the spacer [26] and biofouling control [27]. In pursuit of such properties, a range of chemical surface modifications have been reported, including surface modification using diglyme by plasma polymerization [28], deposition of silver [29] and zinc oxide [30] nanoparticles and organo-selenium [31,32] and CuO [33] coatings. While photocatalytic membranes have been extensively studied, there has been no development of photocatalytic feed spacers thus far, to the best of our knowledge. Immobilization of the photocatalyst on the spacer instead of the membrane can combine the benefits of both suspended and membrane-immobilized photocatalysis. Two additional merits of this approach are: i) membrane degradation due to generation of radicals directly on a photocatalytic membrane surface can be avoided, and ii) The membrane properties can be independently optimized for permeability and selectivity, without being compromising by the photocatalytic coating.

Therefore, inspired by the earlier mentioned work of Lv et al. [22], in this study we developed a new concept for 3D printed feed spacers coated with a photocatalytic layer of iron (β-FeOOH) nanorods. The printed spacers were based on the triply periodic minimal surface (TPMS) architectures, which we have introduced and demonstrated in previous studies to induce superior flow hydrodynamics in the feed channel [34–36]. Of particular relevance, the TPMS designs have far larger specific surface area, compared to commercial spacer designs, making them excellent candidates for use as catalytic sites. Moreover, the versatility of the chemistry of materials from which the spacer can be printed allows for a wide range of chemical pathways to be explored in the future for catalyses' deposition. Here, a PDA/PEI layer was first deposited on the printed spacer to create active sites for binding Fe^{3+} ions from an aqueous $FeCl_3$ solution for a strong attachment of the iron nanorods layer onto the spacer surface. The modified spacers were thoroughly characterized and then tested to determine their efficacy in removing water-soluble pollutants (methylene blue, 4-nitrophenol) in the feed in both batch and crossflow filtration tests. Finally, we demonstrated, using a range of organic foulants (HA, SA, BSA) in the feed solution, the additional benefit these photocatalytic spacers create in terms of membrane cleaning.

2. Materials and methods

2.1. Materials

Dopamine hydrochloride (Dopa. HCl), branched polyethylamine (PEI; avg. MW: 800 Da), hydrogen peroxide (H_2O_2; 30 % aqueous solution), hydrochloric acid (HCl; 36.5 %), methylene blue (MB), ethanol (C_2H_5OH; 99.95 %), trizma base, sodium alginate (SA), bovine serum albumin (BSA; 66 kDa), humic acid (HA; technical grade) and ferric chloride hexa-hydrate ($FeCl_3.6H_2O$; 97 %) were all purchased from Sigma-Aldrich, Germany. Calcium chloride dihydrate ($CaCl_2.2H_2O$; 98 %) was received from SD Fine Chemicals, India. 4-Nitrophenol (4-NP, ≥99.5 %) was procured from Fluka Analytical, Germany. Sodium hydroxide was purchased from Riedel-de Haën, Germany. All chemicals were used as received without further purification. Synder polyethersulfone ultrafiltration (UF) membrane (MWCO = 30 kDa) was purchased from Sterlitech Co., USA. The UF membranes were rinsed with deionized water and compacted by filtration of deionized water at 3 bar for 1 h before use.

### 2.2. Feed spacers printing and surface modification

The feed spacers were 3D printed using the selective laser sintering (SLS) technology. Formiga P110 printer (EOS GmbH, Germany) was utilized in printing the spacers using a thermoplastic PA2202 black material, which is a pigment filled polyamide powder. The spacers were printed based on the TPMS architecture, designed by the level set approximation technique. The TPMS design selected for this study was the Schwarz Crossed Layers of Parallel (CLP) in the transverse direction. This design (henceforth referred to as tCLP) has previously shown excellent hydrodynamics for increased turbulence and reduced membrane fouling [34–36]. The dimensions of the printed spacer were 3.9 cm × 8.5 cm × 2.3 cm. Since conducting certain surface characterizations (FTIR, XRD, SEM-EDS, contact angle measurement, AFM) was not possible on the curved spacers, flat substrate samples were printed for characterization purposes with identical dimensions to the feed spacers and using the same material (PA2202). Further details about the TPMS spacers and the printing technique can be found in our previous work [34,35].

The surface modification of 3D printed spacer was performed in two steps. In the first step (intermediate layer formation), the spacer was pre-wetted by its immersion in absolute ethanol for 1 h. The spacer was then taken out and excess ethanol was removed using a Kimwipe tissue. Next, the pre-wetted spacer was coated by immersion in 100 mL solution of Dopa. HCl and PEI (1:1 w/w) in 50 mM tris buffer for 24 h at 23 °C. The coated spacer was removed from the coating solution and subsequently placed in a vacuum oven for 3 h at 60 °C. The dry coated spacer was then washed using DI water to remove loosely deposited PDA/PEI coating. In the second step (photocatalytic layer formation), the PDA/PEI-coated spacer was soaked in a beaker containing 300 mL solution of 18 mg mL^{-1} $FeCl_3.6H_2O$ for 3 h to adsorb the Fe^{3+} ions. Then, 150 mL of aqueous HCl solution (10 mM) was added to the mixture, with the spacer still in it. The beaker with its content was then placed on a hot plate (IKA, USA) at 60 °C and kept as such for 24 h to complete a mineralization process and the formation of iron nanorods. After that, the temperature was reduced to 23 °C and the spacer with iron nanorods anchored on it was taken out and vacuum dried at 60 °C for 3 h. The images of the spacers along with a schematic reaction route for the formation of β-FeOOH nanorods are shown in Scheme 1.

The leachability of the iron nanorods from the mineralized feed spacer was determined by soaking the coated spacer in 100 mL of DI water for 1 h while stirring at 500 rpm. After 1 h, the water in the beaker was replaced with fresh DI water. This process was repeated 5 times. The removed water in each step was tested using a UV spectrophotometer (UV-1800, Shimadzu, Japan) at 400 nm wavelength to determine the amount of leached coated material in it. The concentration of Fe in the supernatant solutions after the immersion of the spacers in water over 5 h was determined using the inductively coupled plasma – optical emission spectrometer (ICP-OES, 5100, Agilent Technologies, USA).

2.3. Stand-alone nanocomposites preparation

PDA/PEI and iron (β-FeOOH) nanorods anchored powder nanocomposites were also prepared separately (i.e., as stand-alone, not on a
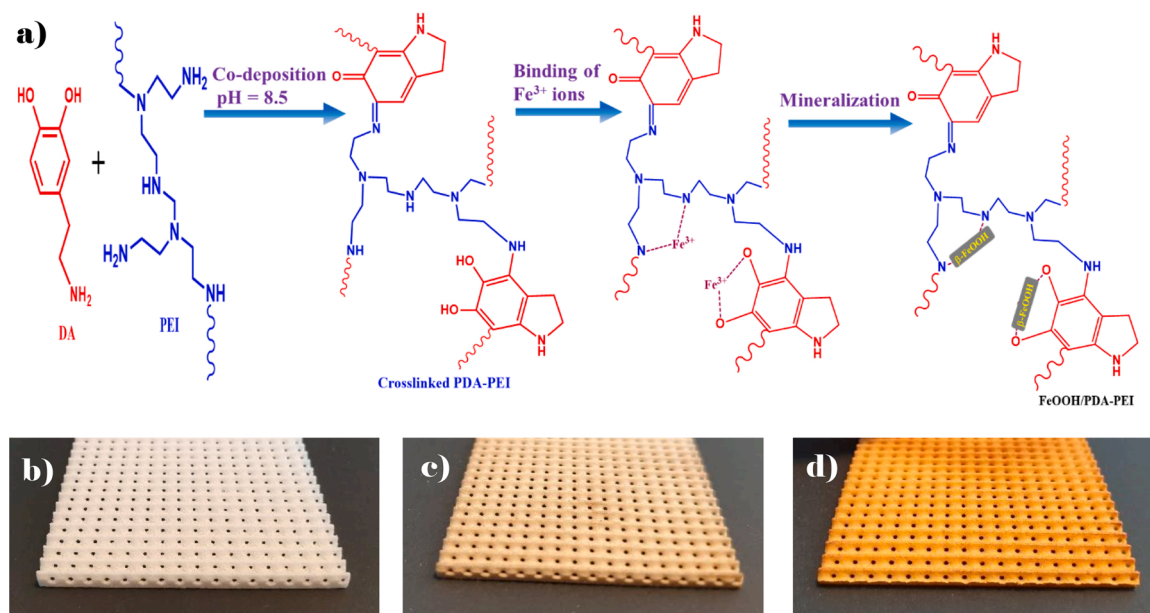
Scheme 1. a) Schematic reaction route for the formation of β-FeOOH nanorods via Mussel-inspired co-deposition of PDA-PEI and mineralization using acidic solution of FeC$_l$ at ambient temperature 60 °C for 24 h; digital photos of b) uncoated spacer; c) PDA/PEI coated spacer; and d) β-FeOOH nanorods coated spacer.

spacer), for the purpose of their characterization. PDA/PEI was synthesized from Dopa. HCl and PEI (1:1 w/w) in 50 mM tris buffer solution. Mussel-inspired polymerization of Dopa in the presence of PEI was carried out in a conical flask at 23 °C. A dark brown suspension was obtained after 24 h *in-situ* polymerization, which was further heated at 60 °C for 3 h. A residue was formed and settled at the bottom of the flask. The reaction mixture was then cooled to 23 °C and centrifuged at 5000 rpm to obtain the precipitated material. The separated precipitant was washed trice by dispersing and centrifuging in DI water and absolute ethanol, sequentially, for 30 min each at 6000 rpm. The solid material was then dispersed again in ethanol and collected on a Whatman filter paper using a vacuum-suction system. The obtained PDA/PEI was then dried in airflow fume hood and subsequently moved into a vacuum oven for further drying at 60 °C until a constant weight was achieved. Next, 100 mg of PDA/PEI, in powder form, was dispersed in 30 mL FeCl$_3$.6H$_2$O solution (18 mg mL^{-1}) and left for 24 h without stirring. The suspension was then filtered and the collected material was mixed with 10 mL HCl aqueous solution (10 mM). The flask and its content was kept on a hot plate at 60 °C for 24 h. Finally, the iron-nanorod-loaded material was separated by centrifugation and washing three times with DI water. The washed material was dried in a vacuum oven at 60 °C and stored in a Ziploc plastic bag until further characterization.

2.4. Materials and surface characterizations

Wide-angle X-ray diffraction (WXRD) was used to record the crystalline structure of the powder material and the prepared feed spacers using an XRD PANalytical Empyrean diffractometer, with a Cu Kα radiation of 1.54 Å at 45 kV and 40 mA, at a scan step size of 0.0170°. The WXRD data for each sample were recorded in a 2θ scan range 10 to 60°.

An attenuated transform reflection-Fourier transform infrared (ATR-FTIR) spectrometer (VERTEX, 80/80v, Germany) was utilized to record the FTIR spectra of powder samples and modified spacers, in the range 4000 to 500 cm^{-1}. The resolution was ±4 for 128 scans of each sample.

Atomic force microscopy (AFM) images were obtained using an AFM microscope (CSI, France) with a silicon cantilever in tapping mode. AFM images were recorded for a scanning area of 3 μm x 3 μm, and were further analyzed using the Gwyddion software (version 2.56) to determine the average roughness (R$_a$; nm), the root mean square of roughness (R$_{ms}$; nm) and the mean difference values between the highest peaks and

the lowest valleys (R$_{max}$; nm).

A field-emission scanning electron microscope (FESEM; Quanta 3D, FIB) was utilized to visualize the surface morphology of both powder samples and modified spacers. The samples were first fixed on the metallic SEM stubs with double-sided carbon tape. Then, the sample was sputter-coated with a 10 nm layer of Au-Pd, after which the surface images were recorded on FESEM at an acceleration voltage 5 kV and 2.0 μm scanning size. The elemental mapping of each sample was conducted using energy dispersive X-ray (EDX) probe attached to the FESEM. A transmission electron microscope (TEM) was used to observe the β-FeOOH nanorods at a higher resolution. The coated spacer was sonicated for 6 h in a 2-propanol solution (100 mL) to dislodge some of the attached nanorods. The solution was then concentrated by heating to increase the β-FeOOH nanorods in the liquid, and was observed under the TEM.

The static and dynamic water contact angles (CA) for PDA/PEI and PDA/PEI- β-FeOOH modified flat substrates were measured using a drop shape goniometer (Easy Drop DSA20E, Krüss, Germany). Each sample was initially dried at 23 °C for 24 h and then fixed on a metallic stand with a double-sided carbon tape. Then, a 5 μL drop of DI water was dropped from a micro-syringe on the top surface and the CA was measured until no further change was noticed. To minimize the experimental error, at least three measurements were performed at different random locations for each sample and the average values were reported.

UV–vis spectrophotometer (UV-2600, Shimadzu, Japan) was used to determine the diffuse-reflectance spectra of the coated flat samples in the range of 200–800 nm. Photoelectrochemical measurements were carried out using a Metrohm Autolab PGSTAT302 N Potentiostat in a standard three-electrode cell with the sample deposited on fluorine doped tin oxide (FTO) as the working electrode, platinum electrode as the counter electrode, and Ag/AgCl electrode as the reference electrode. The electrolyte solution was 0.5 M Na$_2$SO$_4$. Photocurrent transients were recorded at a potential of 0.8 V vs Ag/AgCl electrode. Electrochemical impedance spectroscopy (EIS) was performed in dark and under UV–vis illumination in the frequency range of 0.1 Hz to 10 kHz with an applied potential of 0.8 V vs Ag/AgCl electrode. A 50 W light-emitting diode source with an emission centered at 382 nm was used for irradiation. The average values of the radiation reaching the sample surface, measured with a DeltaOhm 9721 radiometer and matching probes, were 52.8 and 41.6 W/m^2 in the 315 − 400 and 450 − 950 nm

ranges, respectively.

For the stand-alone nanocomposites powder samples, two additional characterizations were carried out. Thermogravimetric analysis (TGA) was conducted in the 30–800 °C range at a 10 °C/min heating rate under N_2 gas flow using a PerkinElmer TGA 4000 thermal analyzer. Differential scanning calorimetry (DSC) was performed from 25 °C to 400 °C at a rate of 10 °C/min in a nitrogen atmosphere using a PerkinElmer DSC 4000.

2.5. Photocatalytic spacer performance

The photocatalytic activity of the feed spacers was assessed in two types of studies: (i) degradation of water soluble organic compounds, both in batch and continuous (filtration) modes, and (ii) membrane surface cleaning by degradation of absorbed and deposited foulants. Details of these two types of tests are provided next.

2.5.1. Degradation of water soluble organic compounds

2.5.1.1. Batch tests. The efficacy of the coated spacer in degrading water soluble compounds was first studied in batch mode. In these tests, a 4cm × 2cm feed spacer specimen was immersed in a glass beaker containing an MB solution and subjected to artificial sunlight from a solar simulator (Newport Corporation, CA, USA) equipped with a Xenon lamp (Ushio, Xenon UXL-16SB, XE 1600 W). The sample beaker was placed at a fixed distance of 30 cm from the light source in all tests. At this distance, the irradiance in the range of wavelength 315–400 nm was 159.7 W/m^2, and in the wavelength range of 400–700 nm it was 6.61×10^3 μmol/m^{2}s. Five different sets of test conditions, covering different combinations of spacer modification, solar light irradiation and H_2O_2 presence in the feed, were applied, as shown in Table 1. In each experiment, 200 mL of a 10 ppm MB solution in DI water was used, to which 30 μL of H_2O_2 (30 % w/v aqueous solution) was added, when applicable (see Table 1). The experimental sets include two control experiments which were performed in the absence of either light (MB 10-C) or H_2O_2 (MB 10-D). Another control test (MB 10-E) was conducted to track the photocatalytic degradation of MB in the absence of a spacer but with H_2O_2 in the solution. The non-reactive adsorption of MB on the spacer surface was accounted for in each test by allowing the immersed spacer to remain in contact with the MB solution in darkness for 1 h before the start of the test, followed by measuring the MB concentration in solution at the end of this period. Afterwards, solar light was allowed to irradiate the beaker, with the spacer in it, and a sample was taken from the solution every one hour afterwards. The concentration of MB in the solution was determined using a UV–vis spectrophotometer (UV-1800, Shimadzu, Japan) by measuring the absorbance at a wavelength of 664 nm.

Batch mode experiments were also conducted using a 25 ppm MB solution and a 10 and 25 ppm solutions of 4-Nitrophenol (4-NP) in water, using modified and unmodified spacers and following the above mentioned protocol with solar light irradiation applied as described above and H_2O_2 present in the feed. For the 4-NP tests, a stock of 200 ppm 4-NP in DI water solution was initially prepared, from which either a 10 or 25 ppm solution was made by further dilution. The concentration of 4-NP in solution was determined using the UV

spectrophotometer by measuring the absorbance at 400 nm, after addition of a base solution (0.5 M NaOH). All the said batch tests were conducted in duplicates and average values were reported.

The complete degradation of MB and 4-NP was also measured in terms of their removal from a 25 ppm solution by measuring the chemical oxygen demand (COD) of the solution. The COD was quantified using a DR3900 UV/Vis spectrophotometer (HACH, USA), employing LCI 500 COD detection cuvettes (HACH, USA).

2.5.1.2. Filtration tests. Upon obtaining the results from the batch tests, decomposition of water soluble organics was studied in a crossflow filtration operation at constant trans-membrane pressure (TMP). A schematic of the photocatalytic filtration setup used in this study is shown in Scheme 2 and is briefly described here. The membrane and the spacer were housed in a flat-sheet CF042 acrylic flow filtration cell (Sterlitech Co., Kent, WA, USA). The cell had outer dimensions of 12.7 × 10 × 8.3 cm^3, inner dimensions of 9.21 × 4.57 cm^2 and a feed channel depth of 2.3 mm. The cell was integrated with a Poseidon filtration system (Convergence B.V. Co., The Netherlands), which had an operational flow range of 0−30 L/h and pressure range of 0−5 bar. The earlier mentioned solar simulator was used as the solar light source, with the same operating distance as the batch tests. The filtration cell was placed at a fixed distance of 30 cm from the light source for all tests. 30 μL of H_2O_2 (30 % w/v aqueous solution) was added to the feed solution in each experiment. The filtration system was operated in a closed loop (i.e., the permeate and retentate were both returned to a feed reservoir). As such, the reduction in solute concentration in the feed was attributed to photocatalytic degradation.

Initially, the filtration system was flushed with DI water. Feed solution of known concentration was then circulated in the system without the membrane or spacer in order to reach a uniform solute concentration in the system pipes. The membrane and spacer were then inserted in the filtration cell and the system was operated at a feed flow rate of 10 L/h and TMP of 1 bar. During the first hour of feed circulation, the adsorption of MB or 4-NP on the spacer and membrane surface was allowed to take place in darkness, similar to the batch tests. After the adsorption reached equilibrium and a stable feed concentration was attained, H_2O_2 was added to the feed reservoir and the solar simulator was turned on. The concentration of solute in the feed reservoir was also measured at that point and at one hour intervals thereafter. The organics degradation tests under filtration mode were carried out for 10 and 25 ppm MB and 10 and 25 ppm 4-NP feed solutions.

2.5.2. Membrane surface cleaning

The impact of the spacer's photocatalytic activity on the membrane surface cleaning was verified in two ways. First, the used membranes from the earlier mentioned organics degradation test, under filtration mode using 10 ppm MB, were analyzed to determine the relative degree of MB adsorption on the membrane surface, when uncoated and photocatalytic spacers were used. For that, the membranes were dried at the end of the test and analyzed in a UV–vis spectrophotometer (UV-2600, Shimadzu, Japan) to determine the diffuse-reflectance spectra from 400 nm to 800 nm. These spectra were compared with the spectra of the membrane at the end of the adsorption phase (i.e., before photocatalysis), to determine the relative degree of membrane surface cleaning using uncoated and photocatalytic spacers.

Second, membrane cleaning via the removal by photocatalytic spacers of foulants adsorbed/deposited on the membrane surface was studied during an ultrafiltration (UF) process. Three of the most commonly utilized foulants in UF fouling studies; BSA, HA and SA, were herein used. A 10 ppm solution of each solute was prepared and dosed with 0.5 mM calcium chloride. This dosing was done for two reasons: (i) the presence of Ca^{2+} ions represent natural conditions found in surface water and (ii) presence of Ca^{2+} ions in solution is known to contribute to aggravate the fouling by BSA, HA, and SA [37,38], making this a more

Table 1
Test conditions applied in water soluble chemical degradation tests in batch and filtration modes (feed: 10 ppm MB in DI water).

Photocatalysis test	Spacer	Coating	H_2O_2	Light
MB 10 – A	✓	✓	✓	✓
MB 10 – B	✓	×	✓	✓
MB 10 – C	✓	✓	✓	×
MB 10 – D	✓	✓	×	✓
MB 10 – E	×	×	✓	✓
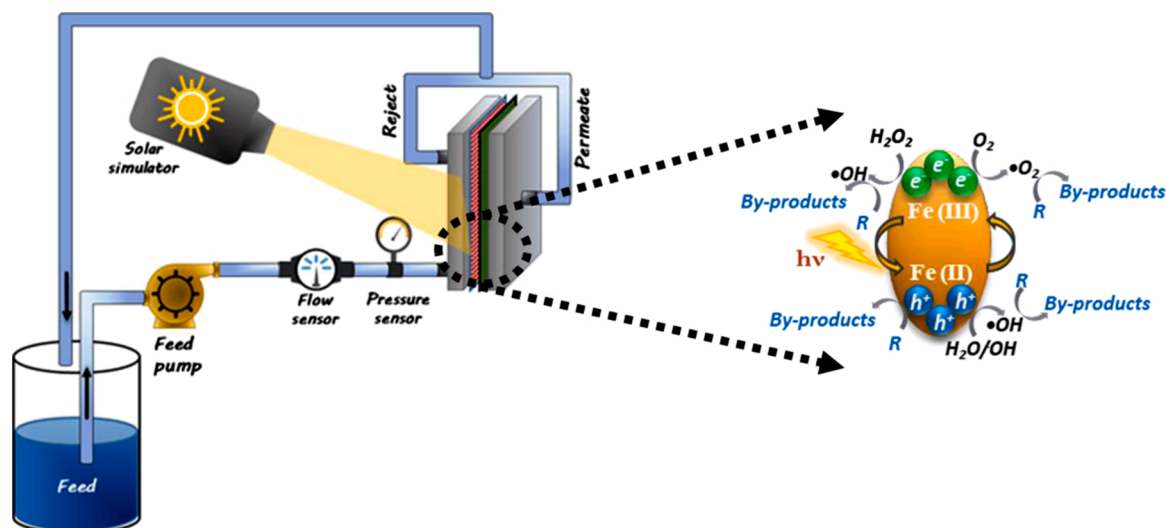
Scheme 2. Schematic of the photocatalytic setup consisting of filtration system and solar simulator as light source and photocatalytic activity in β-FeOOH nanorods.

challenging fouling condition. The earlier described filtration setup was used in these tests. The experimental protocol of these studies is as follows: the membrane was first pre-compacted by filtering DI water for 1 h under a TMP of 3 bar, after which the pure water permeability (PWP) of the pristine membrane (PWP$_{pristine}$) was measured at 2.5 bar TMP. Next, the feed tank was filled with a feed solution containing 10 ppm of one of the three foulants and 0.5 mM CaCl$_2$. The solution was then fed to the membrane cell, without solar light, at a flow rate of 10 L h^{-1} and TMP of 2.5 bar for 2 h. The membrane flux was continuously measured during this period. At the end of the 2 h, the unused feed solution was discarded and the feed tank was filled with DI water and the pure water permeability of the fouled membrane (PWP$_{fouled}$) was measured. Then, 100 μL H$_2$O$_2$ was added to the DI water in the feed tank and the mix was fed to the filtration cell, with the solar light switched on, for 30 min to activate the photocatalytic cleaning of the fouled membrane. At the end of the 30 min, the unused solution in the feed tank was discarded and the tank was filled with DI water again. Then, pure water permeability of the cleaned membrane (PWP$_{cleaned}$) was measured. The membrane cleaning efficiency was determined using the resistance in series model [39]. According to this model, the membrane flux can be expressed as:

$$J = \frac{\Delta P}{\mu (R_m + R_f)} \quad (1)$$

Where ΔP (Pa) is the transmembrane pressure (TMP), μ (Pa.s) is the viscosity of the permeate, R$_m$ (m^{-1}) is the intrinsic resistance of the membrane and R$_f$ (m^{-1}) is the overall fouling resistance. The combination of R$_m$ and R$_f$ (R$_m$+R$_f$) is referred to as the total resistance, R$_{tot}$ (m^{-1}). R$_{tot}$ and R$_m$ were calculated using the following equations:

$$R_{tot} = \frac{1}{\mu.PWP_{fouled}} \quad (2)$$

$$R_m = \frac{1}{\mu.PWP_{pristine}} \quad (3)$$

By difference, R$_f$ ($_{(}$ m^{-1}) was calculated as:

$$R_f = R_{tot} - R_m \quad (4)$$

The cleaning efficiency was expressed in terms of the flux recovery ratio (FRR, %), defined as:

$$FRR \ (\%) = \frac{PWP_{cleaned}}{PWP_{pristine}} \times 100 \quad (5)$$

2.5.3. Cyclic membrane cleaning tests

The stability and reusability of the coated spacer was tested by performing membrane cleaning tests over 4 cycles. The cyclic tests were carried out using a modified CF042A cell from Sterlitech, which has a 2cm × 2cm acrylic cut-out in the middle of the cell (Figure S11, SI), in order to increase the transmission of light through the feed cell.

Following an initial membrane compaction with DI water for 1 h at a TMP of 3 bar, the permeability of the pristine membrane was measured. For each cycle, a 10 ppm solution of HA was prepared and dosed with 0.5 mM calcium chloride. The filtration was performed at a flow rate of 10 L h^{-1} and TMP of 2 bar for 1.5 h in the absence of solar light. The permeability of the fouled membrane was measured, following which the light was switched on for 30 min and H$_2$O$_2$ in DI water was dosed to the membrane cell. The permeability of the membrane post the photocatalytic cleaning was measured, which concluded the first cycle. Next, a new feed solution of HA was used to carry out the filtration for the second cycle. This was repeated for a total of 4 cycles. After completing the 4 cycles, the membrane was removed from the cell and dried. The cross-section of the fouled membrane was visualized and compared with that of the pristine membrane.

3. Results and discussions

3.1. Nanocomposite material characterization

The FTIR spectra of PDA/PEI and β-FeOOH anchored PDA/PEI nanocomposites are presented in Figure S1 (Supplementary Information, SI). For the PDA/PEI nanocomposites, the peaks at 1665 cm^{-1}, 1580 cm^{-1}, 1560 cm^{-1} and 1487 cm^{-1} are associated with stretching vibrations of C═N, N—H and C═C groups [40]. The vibration peak of the O—H at 3400 cm^{-1} becomes strong after the nanorods mineralization [22]. This is due to the formation of FeOOH and the increased presence of O—H bonds in the nanocomposites after mineralization. The characteristic peak for the β-FeOOH anchored PDA/PEI nanocomposites at 1000 cm^{-1} corresponds to the stretching vibration of Fe−O moiety [20].

Figure S2 (SI) shows the TGA data for PDA/PEI and β-FeOOH−PDA/PEI nanocomposite. It can be seen that a 70 wt.% loss in mass of β-FeOOH was observed at 800 °C, which is attributed to the conversion of β-FeOOH to Fe$_2$O$_3$ via a continuous dehydration with the increasing temperature in the 100–800 °C range [41,42]. The adsorbed amount of water can be correlated to the extent of catalytic activity, with the water assisting with the dissolution and dissociation of the reactive species during catalysis [43,44]. The PDA/PEI, on the other hand, was

completely decomposed at 800 °C. This signifies the increased thermal stability of the β-FeOOH−PDA/PEI nanocomposite, as expected from the inorganic compound. Figure S3 (SI) shows the DSC results of PDA/PEI and β-FeOOH−PDA/PEI nanocomposite. The DSC curve for the PDA/-PEI nanocomposite shows a sharp exothermic peak at 160−170 °C which is the crystallization temperature (T_C) of the polymer [45]. For the β-FeOOH−PDA/PEI nanocomposite, the endothermic peak at ~100 °C corresponds to the loss of water from the hydroxide bonds of the FeOOH, while the exothermic peak from 200 °C to 300 °C can be assigned to the decomposition of precursors present in the sample as well as the conversion of β−FeOOH to Fe_2O_3 [46].

The SEM-EDX spectra of PDA/PEI and β-FeOOH−PDA/PEI nanocomposite (Figure S4, SI) provide additional confirmation of the successful anchoring of β-FeOOH nanorods on the PDA/PEI nanocomposite, by showing iron being present in the β-FeOOH nanorods sample and absent in the PDA/PEI sample. Chlorine is detected in both samples due to the presence of dopamine hydrochloride residue.

3.2. Spacer coating characterization

XRD and ATR-FTIR characterization tools were utilized to confirm the successful anchoring of β-FeOOH nanorods on the 3D printed flat substrate. The XRD patterns of uncoated, PDA/PEI and β-FeOOH coated flat substrates are shown in Fig. 1a. The diffraction peaks in all substrates at 20°, 23°, 37° and 40° are present because of the base polyamide material [47,48]. New peaks appeared at 12°, 17°, 27°, 34°, 35° and 56° in the XRD pattern of β-FeOOH coated substrate, which correspond to the crystal structure of the FeOOH nanorods [49]. This confirms the successful growth and presence of β-FeOOH nanorods (JCPDS No. 34 − 1266) on the modified substrate [22]. Similarly, the ATR-FTIR spectra in Fig. 2b show a characteristic peak at 3500 cm^{-1} due to O—H stretching vibrations. This significant peak appears only in the case of β-FeOOH coated substrate, as expected. The other peaks are associated with the polyamide material and are common for all three samples [50, 51].

Figs. 1c and 1d show the dynamic and static water contact angle (CA), respectively, for the uncoated, PDA/PEI and β-FeOOH coated flat substrate. It was observed that the surface became progressively more hydrophilic with PDA/PEI coatings and more so with β-FeOOH anchoring, which is in line with the changes reported in literature previously [22]. The increased surface hydrophilicity is due to the inherent hydrophilicity of the inorganic β-FeOOH and the hydroxide groups present at the surface of the substrate [52]. Typically, the contact angle of a surface is strongly affected by the surface roughness. A rougher surface is usually more hydrophobic. However, even though the β-FeOOH significantly increases the surface roughness, it also increases the hydrophilicity. Increased hydrophilicity is also typically associated with reduced fouling in membrane systems [23].

The UV–vis diffuse-reflectance spectra for the samples are given in Fig. 1e. Band gap values were calculated from the reflectance. Addition of the PDA/PEI layer coating to the polyamide substrate (i) considerably enhanced the absorption of both UV + visible light, (ii) significantly reduced the optical band gap, and (iii) expanded the absorption band edge from ca. 420 to 680 nm. A slight loss in optical absorbance, a small increase in band gap, and a minor reduction in the band edge were observed with the addition of the β-FeOOH coating. The shift in the absorption band edge from ca. 680 to 640 nm and the increase in band gap from 1.58 to 2.00 is due to β-FeOOH nanorods. Pure β-FeOOH has an absorption band edge at ca. 570 nm and a band gap that ranges from 1.9 to 2.2 eV, which explains why the band gap of PDA/PEI increased after coating and why the band edge decreased. A new optical absorption shoulder appeared at ca. 500 nm. This is a result of the pair excitations of two neighboring Fe^{3+} cations, which was induced by the introduction of β-FeOOH. This may be used to further confirm the successful growth of β-FeOOH. Next, the β-FeOOH nanorods are successfully visualized in the TEM image (Fig. 1f).

The transient photocurrent results are shown in Figure S5, SI. Both PDA/PEI and β-FeOOH coatings can generate current in the dark, but the current generated is higher under light irradiation (especially for samples without β-FeOOH coating). The addition of β-FeOOH nanorods enhanced the current density in the dark but reduced it under light. Similarly, for the electrochemical impedance spectroscopy, the addition of the β-FeOOH nanorods increased the charge transfer resistance. According to Huang et al. [53], pure FeOOH was shown to exhibit a rapid recombination of photo-induced charges and this may be used to explain the lower photocurrent density and the higher charge transfer resistance with the FeOOH coating. However, according to Wang et al. [54], FeOOH should have enhanced the photocurrent density and lowered the resistance of charge transfer by promoting the separation of charges and hence the transport of electrons. One reason for the contradicting result may be that the PDA/PEI film was much more uniformly deposited onto the FTO substrate, while the β-FeOOH nanorods were attached haphazardly. It is also worth noting that the photocurrent is measured in the absence of the dye. Adsorption of the dye may be more efficient in the presence of β-FeOOH as the dye can adsorb better on β-FeOOH rather than on the polymer. Metal-to-ligand charge transfer to the dye can be more effective in the presence of β-FeOOH which can exchange energy and electrons better with the organic moieties of the dye.

The surface morphology and SEM-EDX spectra of uncoated, PDA/PEI coated and β-FeOOH nanorods anchored 3D printed substrates are displayed in Fig. 2 (a, b and c, respectively). The β-FeOOH nanorods, which are ∼ 200−400 nm in length, grow without a specific orientation on the surface of PDA/PEI coated substrate. The EDX spectra reveal that, compared to the uncoated and PDA/PEI coated substrates, new peaks at 0.70, 6.38 and 7.03 KeV were visualized in the spectrum of β-FeOOH-coated substrate, which are attributed to Fe Lα, Fe Kα and Fe Kβ, respectively. Due to the formation of β-FeOOH nanorods, the O/C ratio increased from 0.20 for the PDA/PEI coated substrate to 0.25 for the β-FeOOH-coated substrate. The peaks present from 1 to 4 keV represent impurities such as Si, and Cl due to the residues of dopamine hydrochloride used in the coating of PDA/PEI layer.

The elemental mapping data for uncoated and coated substrates further validates the formation and homogeneous distribution of β−FeOOH nanorods over the β-FeOOH-coated substrate (Figure S6 SI). A cross-sectional SEM image of β-FeOOH nanorods coated spacer is shown in Figure S7 (SI). The sample was prepared by slicing the coated spacer to reveal the uncoated inner polyamide substrate, with the β−FeOOH coating on the top surface. Elemental mapping was performed on the sample to reveal regions of high Fe content and regions without Fe content. The mapping demonstrates the presence of Fe exclusively on the surface of the spacer while being absent from the inner spacer material.

The root-mean-square roughness (R_{rms}; nm) values for uncoated, PDA/PEI and β-FeOOH coated flat substrates were determined using AFM and the obtained images for the two-dimensional and three-dimensional morphologies are shown in Fig. 3. R_{rms} slightly increased from 33.8 nm to 35.1 nm after coating the surface of polyamide substrate with the PDA/PEI layer. A more significant increase in R_{rms}, from 35.1 nm to 84 nm, was noticed after the growth of β-FeOOH nanorods on the surface of PDA/PEI coated substrate. The random growth of the β-FeOOH nanorods on the surface, with each nanorod being ∼ 200−400 nm in length (Fig. 2), led to this significant increase in surface roughness. Table 2 shows additional surface roughness details, including the average roughness (R_a) and maximum height (R_{max}) of the three samples. A similar trend to that of R_{rms} is observed in R_a and R_{max}, whereas a significant increase has occurred upon the coating with the β-FeOOH nanorods. It is worth mentioning that the additional surface roughness is beneficial to the catalytic activity of the coated layer since it means increased surface area, which is typically beneficial for catalysis [55].

Finally, leaching tests were conducted in water, as described in Section 2.1, to confirm the stability of the β−FeOOH nanorods and their
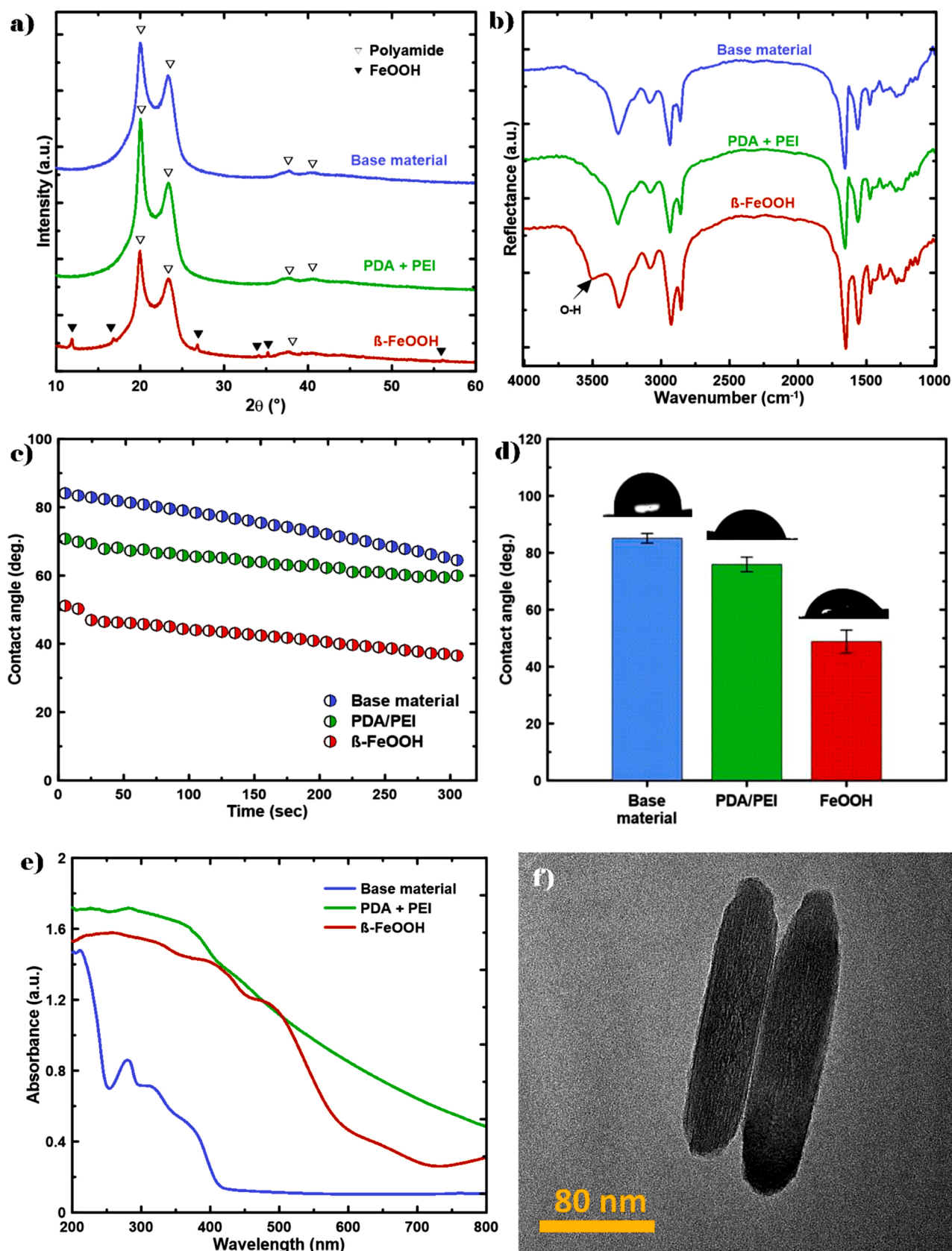
Fig. 1. a) XRD pattern of the base material, PDA/PEI layer and β-FeOOH coating; b) DRIFT/FT-IR spectra of base material, PDA/PEI layer and β-FeOOH coating c) dynamic contact angle measurements of the base material, PDA/PEI layer and β-FeOOH coating; d) static contact angle measurements of the base material, PDA/PEI layer and β-FeOOH coating; e) diffuse-reflectance spectra of the base material, PDA/PEI layer and β-FeOOH coating; f) TEM image of β-FeOOH nanorod.
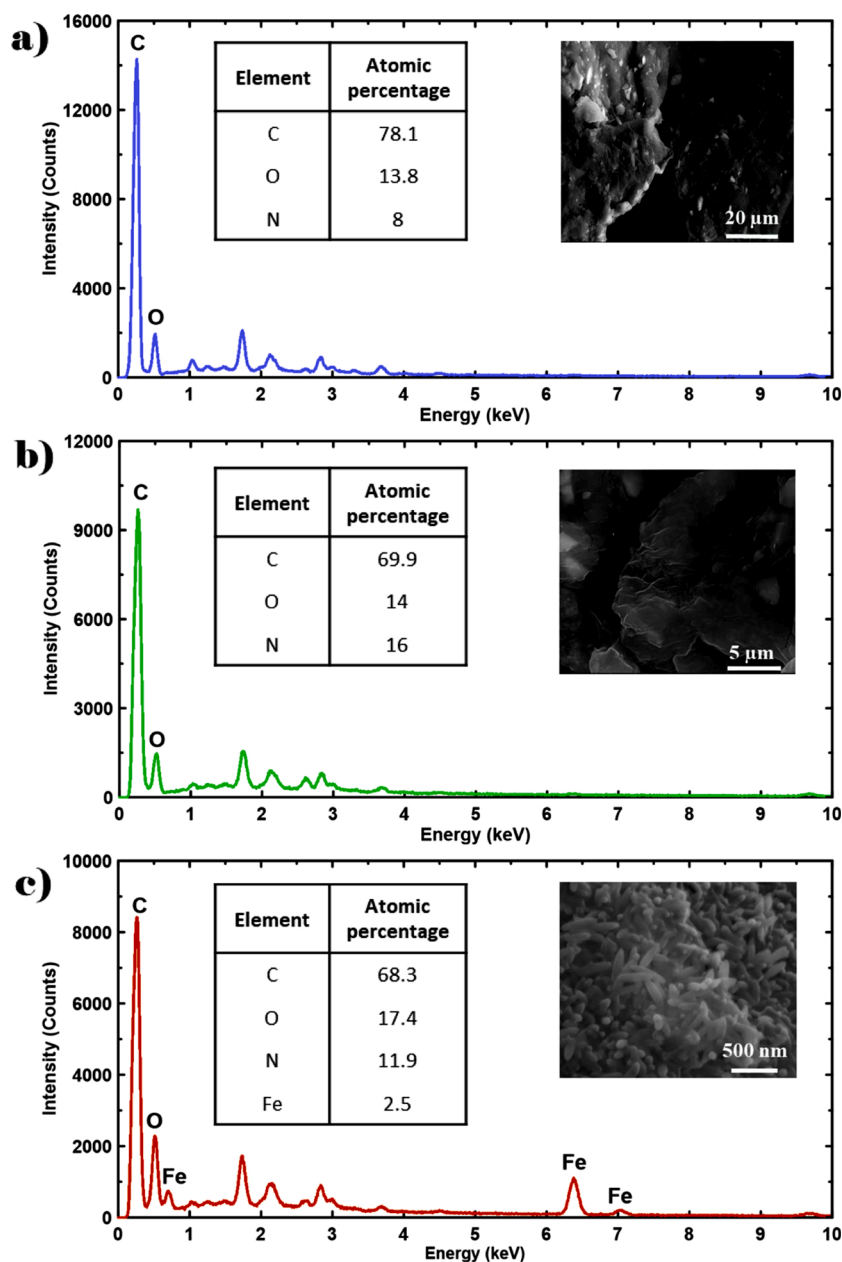
Fig. 2. EDX spectra of a) the base 3D printed polyamide substrate; b) base material coated with PDA/PEI intermediate layer; and c) base material with final β-FeOOH nanorods coating. Insets show the SEM image for the different samples.

attachment to the PDA/PEI layer underneath. After one hour of immersion in water under stirring, the absorbance of the supernatant solution was 0.4 at wavelength of 400 nm (Figure S8, SI), owing to leaching of weakly adhered β−FeOOH nanorods from the substrate surface during stirring. The absorbance decreased drastically to 0.05 after the second hour and was almost negligible after that up to five hours of immersion and stirring. Similarly, the Fe concentration determined by ICP-OES decreases drastically from 82 ppm in the first hour to 7.5 ppm in the second hour, while dropping to 1 ppm subsequently. The SEM images of the surface taken pre- and post-washing demonstrate that the density of nanorods on the surface of coated spacer surface remains intact. This suggests that the strongly bound β−FeOOH nanorods remained intact on the surface of modified substrate. This indicates that the coordination between Fe^{3+} of the β−FeOOH nanorods and the catechol moieties of the PDA/PEI coating layer has yielded a strong attachment of the nanorods to the surface of the 3D printed substrate. The initial high concentration of leached nanorods in the supernatant

solution after the immersion of coated spacer in water could come from the loosely attached nanorods in the grooves and crevices of the spacer, which are dislodged easily.

3.3. Photocatalytic degradation of organic compounds in water

3.3.1. Batch tests

The efficiency of photocatalytic degradation of organics in the aqueous feed by the iron nanorods-coated spacers was first tested in static batch mode using 10 ppm MB solution. These control tests were carried out to examine the impacts of different parameters relevant to the photocatalytic degradation process (see Table 1) and their results are presented in Fig. 4a. In the MB10−A test, a β−FeOOH coated spacer was used with H_2O_2 and solar light. In this test, the maximum MB removal among all batch tests (98 %) was achieved after 3 h of exposure to light. In comparison, the removal rate for MB after 3 h in test MB10−B (uncoated spacer, with H_2O_2 and light) was 93 % and that in MB10−E (no
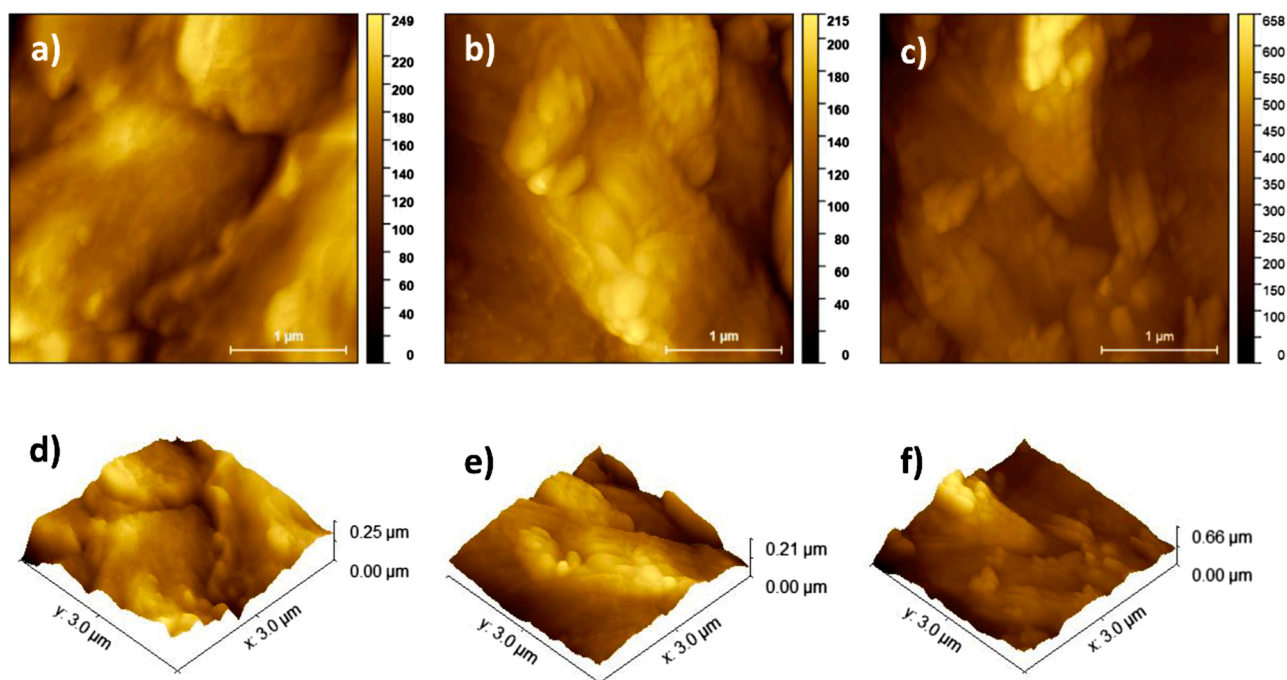
Fig. 3. Top row: AFM images showing two-dimensional surface morphology of a) the base material; b) PDA/PEI intermediate layer; and c) β-FeOOH nanorods coating. Bottom row: AFM images showing three-dimensional surface morphology of d) the base material; e) PDA/PEI intermediate layer; and f) β-FeOOH nanorods coating.
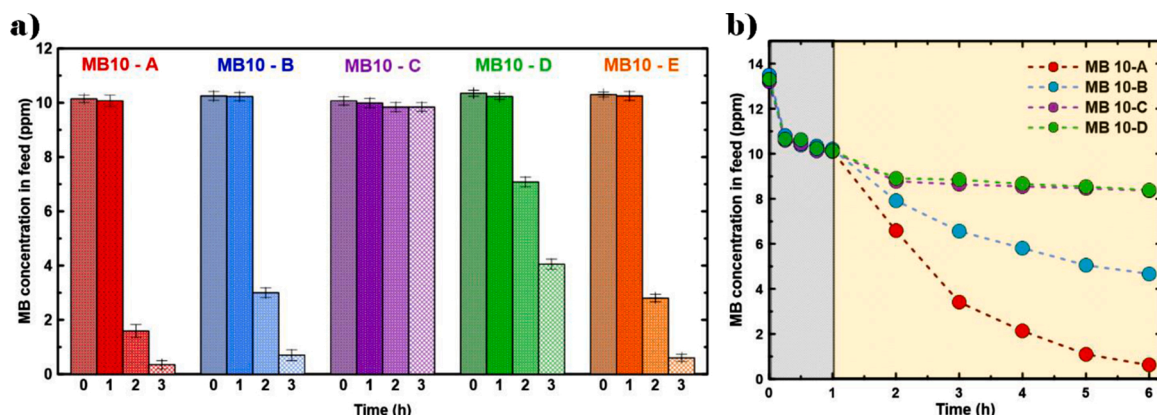
Table 2
Surface roughness analysis from AFM of the coated surfaces.

Sample	R_a (nm)	R_{ms} (nm)	R_{max} (nm)
Base material	26.94	33.80	249.5
PDA/PEI	29.32	35.12	214.6
β-FeOOH	60.44	84.04	658.0

spacer, with H_2O_2 and light) was 94 %. While in the latter two cases the MB removal rate was lower than when a coated spacer was used, the improvement in photocatalytic degradation that can be attributed to the nanorods coating was small and a significant removal of MB was still achievable by solely using solar irradiation and H_2O_2. As will be shown next, the nanorods contribute to a far more pronounced difference in performance when a higher organics concentration is used or when the photocatalysis takes place under a continuous filtration mode. As expected, the absence of H_2O_2 reduced the removal rate using the coated spacer to only 61 % (test MB10-D), while the complete absence of light in the MB10−C test made the removal of MB impossible.

To investigate the potential advantage of β−FeOOH coated spacer when dissolved organics are present at higher concentration in solution, additional batch tests were conducted to study the photocatalytic degradation of a 25 ppm MB solution (Fig. 5a). In this case, the coated spacer was found effective in removing 98 % of MB over a 4 h test, compared to only 70 % removal by the uncoated spacer, using solar light and in the presence of H_2O_2. These results demonstrate the role of β−FeOOH nanorods coating as a catalyst in photocatalytic degradation of MB. Building on the MB removal results, the β−FeOOH coated spacers were tested for the degradation of 4-NP, a chemically stable organic pollutant that is hazardous to both human health and the environment [56]. The β−FeOOH nanorods coated spacer was first applied in the photocatalytic degradation of 10 ppm solution of 4-NP, where it was able to remove 98 % of 4-NP (Fig. 5c). This is significantly higher that the corresponding removal rate for the same solution using an uncoated spacer (77 %). When testing the uncoated and coated spacers for the removal of 4-NP at a higher (25 ppm) concentration, the advantage of the coated spacer was even more evident. The removal rate using the coated spacer was 98.8 % in this case, while the uncoated spacer was

Fig. 4. Photocatalytic tests for a) batch mode and b) filtration mode photocatalysis, using 10 ppm MB solution under the various test conditions shown in Table 1.
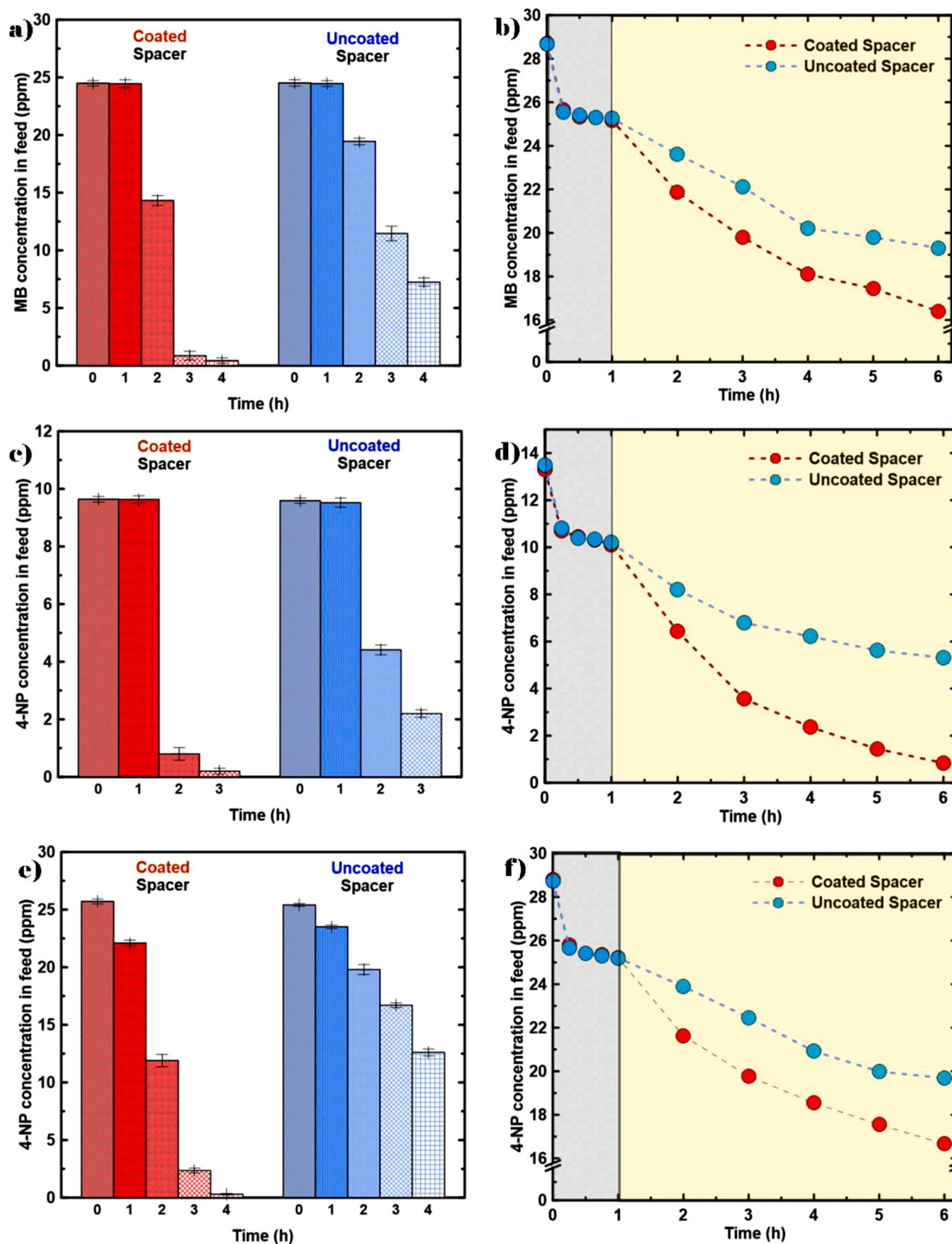
Fig. 5. Batch mode and dynamic filtration mode photocatalytic degradation tests of 25 ppm MB solution (a & b, respectively), 10 ppm 4-NP solution (c & d, respectively) and 25 ppm 4-NP solution (e & f, respectively). Adsorption of MB or 4-NP on the spacer and membrane (in filtration mode) was allowed to take place in darkness for the first hour, after which a stable feed concentration was achieved and solar irradiation was started. All feed solutions contained 30 μL of H_2O_2.

able to remove only 50.4 % of the 4-NP (Fig. 5e).

The COD removal rate of β-FeOOH nanorods coated spacer was 75.2 % in the case of 25 ppm MB and 71.5 % for 25 ppm 4-NP, compared to 57.6 % and 31.4 %, respectively, using the uncoated spacer (Fig. 6). This proves that the photocatalytic degradation process using the nanorods was capable of the full decomposition of organic carbon to a significant extent. In the presence of electron acceptors such as H_2O_2, Fenton-like reactions occurs with the β−FeOOH which leads to the decomposition of the organic compounds. There are two mechanisms that can occur in a system containing β−FeOOH, H_2O_2 and light. Firstly, there is the potential for ligand to metal charge transfer (LMCT) where the organic material is oxidized by the transfer of the electron from the highest occupied molecular orbital of the organic surface to the conduction band of the semiconducting material. The transfer of electron occurs due to the absorption of photons emitted by the light source. The released electron reacts with the H_2O_2 in the solution and further radicals are generated. Subsequently, the oxidized organic either degrades or recombines with the electron [15]. In the second mechanism of degradation, electron-hole pairs are generated on the surface of the β−FeOOH nanorods through an irradiation of UV light. The resulting electron-hole pairs further react with H_2O_2 to generate more radicals, which are highly reactive and non-selective in their degradation of organics [57].

Batch tests were also carried out for the stand-alone nanocomposites in order to determine their photocatalytic activity, and the effect of immobilization on a feed spacer. The degradation of 10 ppm MB solution by the PDA/PEI and β−FeOOH nanocomposites is presented in Figure S9, Supplementary Information. The amount of each material used was kept equal to the mass of the β−FeOOH nanorods growth on the feed spacer (23 mg). The degradation of MB by the PDA/PEI nanocomposite was non-existent, as the results were similar to those obtained without the coated spacer in Fig. 4a. In the case of the β−FeOOH nanocomposites, the degradation was slightly lower in comparison with the coated spacer. This can be due to the reduced formation of nanorods on the PDA/PEI nanocomposite surface as well as the uneven shape and size of the particles.

3.3.2. Filtration tests

Based on the promising results of batch tests, the photocatalytic decomposition efficacy of β−FeOOH nanorods-coated spacers was tested in a crossflow dynamic filtration mode. While the majority of previously

Fig. 6. COD removal with uncoated and β-FeOOH coated feed spacer for 25 ppm MB and 25 ppm 4-NP.

reported tests on photocatalytic membranes have been conducted using dead-end filtration setups [58–61], the crossflow dynamic filtration setup represents the majority of commercial membrane filtration systems and is, therefore, herein used. Initially, the spacer's performance was checked under various test conditions, using a 10 ppm MB feed solution. Four out of the 5 test sets presented in Table 1 (MB 10-A, MB 10-B, MB 10-C, MB 10-D) were tested in crossflow filtration mode and the results are shown in Fig. 4b. The highest removal of MB (94 %) from the feed solution was achieved in test MB 10-A after 5 h of photocatalysis, where a coated spacer, solar radiation and H_2O_2 were all applied. The second best was test MB 10-B, achieving a 54 % MB removal rate, using light and H_2O_2 but an uncoated spacer. Interestingly, tests MB10-C and MB10-D, where either light or H_2O_2 was missing, both yielded very low levels of MB removal, 17.2 % for the former and 17.1 % for the latter. In contrast to its corresponding batch test result (Fig. 4a), the test conditions of MB10-D led to far less significant photocatalysis efficiency. This can be explained by considering the reduced transmittance of light through the CF042 acrylic filtration cell, used in the dynamic filtration tests, compared to the transmittance through the glass beaker used in the batch test. As measured by a radiometer, in the range of wavelength 315–400 nm, the irradiance in front of the acrylic sheet on the feed-side was 159.7 W/m^2, which dropped to only 0.339 W/m^2 behind the sheet (where the spacer is positioned during the test). In the wavelength range of 400–700 nm, the irradiance in front of the acrylic sheet was 6.61 × 10^3 μmol/m^{2}s, compared to 2.40 × 10^3 μmol/m^{2}s behind it. The difference in irradiance values in the 315−400 nm wavelength range can be considered mainly responsible for the large difference in photocatalytic degradation between the batch and filtration modes. It is well-known that UV light is more efficient than visible light in producing radicals on the surface of photocatalyst. The shorter wavelength of the UV light comes with a higher energy, which leads to greater photocatalytic degradation [62]. Therefore, the formation of radicals in the feed side of the filtration cell decreased due to the low transmission of UV light, leading to the observed lower photocatalytic degradation rate in crossflow dynamic filtration. Collectively, the filtration test results using 10 ppm MB feed establish that both light and H_2O_2 are essential for the coated spacer to perform its photocatalytic role effectively. Thus, henceforth, all filtration tests were conducted using a coated spacer in the presence of both light and H_2O_2. The filtration test using a 25 ppm MB feed solution (Fig. 5b) lends further support to these findings. The removal rate of MB after 5 h of filtration/photocatalysis was 35 % and 23.5 % for the coated and uncoated spacer, respectively. Unlike the batch mode, where a higher MB concentration led to an increase in its removal rate, the photocatalytic removal rate does not seem to be impacted significantly by feed concentration in filtration mode.

Similarly, degradation of 4-NP in a crossflow dynamic filtration was observed. The removal rate for a 10 ppm solution of 4-NP was 92 % in the case of coated spacer, compared to 47 % for uncoated spacer (Fig. 5d). On the other hand, the removal rates using a 25 ppm 4-NP solution, were 34 % and 21 % for the coated and uncoated spacer, respectively (Fig. 5f). Both tests confirm a significant contribution of a β−FeOOH coated photocatalytic spacer to the degradation of the challenging 4-NP pollutant during a membrane filtration process.

3.4. Membrane cleaning effect

Membrane foulants are external species that affect the membrane performance either through their physical deposition and cake formation on the membrane, or through adsorption onto the membrane surface. The photocatalytic activity of the spacer, thanks to its β−FeOOH nanorods coatings, was found to have a positive effect on the membrane surface, in terms of reducing foulant deposition. The adsorption of MB onto the membrane was initially visually noticed during the filtration of the 10 ppm MB solution. Over the course of the photocatalytic operation of the filtration system, a change in the adsorbed MB on the membrane
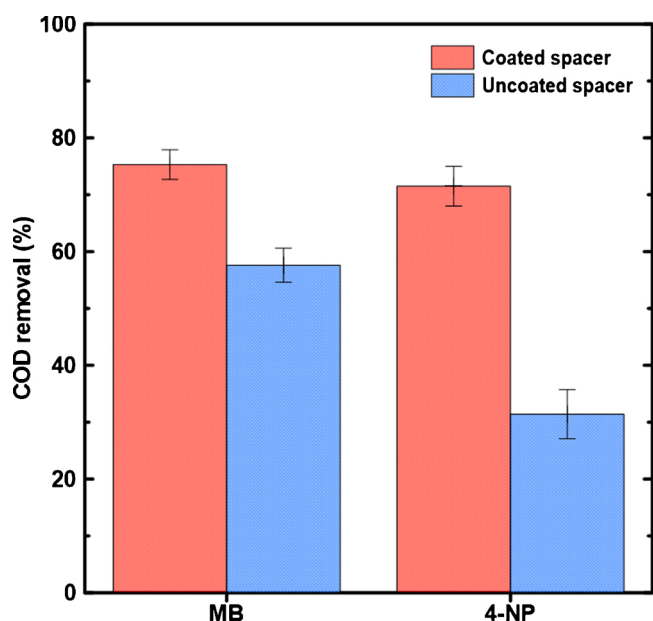
was observed through a change in membrane discoloration, as captured in Fig. 7 (a, b and c). Then, the absorbed MB on the membrane surface was qualitatively assessed using diffuse reflectance spectroscopy (Fig. 7d). Higher reflectance (%) at a given wavelength points to a reduced concentration of MB on the surface. At a wavelength of 664 nm (one characteristic peak of MB), the reflectance prior to photocatalysis (2.4 %) was not significantly different from the reflectance after photocatalysis using the uncoated spacer (3.2 %). However, after photocatalysis using coated spacer, the reflectance significantly increased to 18.2 %, confirming the visual observation of reduced MB absorbance on the membrane surface.

This very interesting impact of the photocatalytic spacer on MB deposition on the membrane itself led to the subsequent investigation of the potential role of photocatalytic spacer as a tool for removing deposits of other well-known organic foulants in water from the membrane surface. Such foulants are typically retained by UF membranes during water filtration processes and are directly responsible for cake layer formation on the membrane, leading to membrane performance decline [63]. Typically, such deposited foulants are washed away via mechanical methods, such as backwash and relaxation, and/or chemical cleaning using sodium hypochlorite, sodium hydroxide, etc. Photocatalytic activation of $\beta-$FeOOH coated spacers offers an alternative to these mechanical and chemical cleaning methods for the tackling of membrane fouling. So, the coated spacers were tested for the removal of three organic foulants; SA, HA and BSA, and the results are discussed next.

During the filtration of a 10 ppm SA solution (Fig. 8a), a gradual drop in permeate flux was observed over time, with flux reaching 27 % of its original value after 2 h of crossflow filtration. This is attributed to the well-studied alginate gel that is formed in the presence of Ca^{2+} ions. However, the permeate flux significantly increased after photocatalytic cleaning was conducted for 30 min via the activation of $\beta-$FeOOH coated spacer through solar light with the addition of hydrogen peroxide (during the photocatalytic cleaning only). This is attributed to the removal of the SA deposited on the membrane via free radicals' generation through the coated spacer. As a consequence, $PWP_{cleaned}$ was 21 % higher than PWP_{fouled}, as also illustrated by the reduction in the overall fouling resistance (R_f) (Fig. 9a) (see the description of these parameters in section 2.5.2). The R_f prior to the cleaning was 1.54 m^{-1}, which was reduced by 75 % after cleaning. In addition, the efficiency of the coated spacer in the degradation of cake layer on the membrane was verified by

the high FRR value of 92 % (Fig. 9b). A control test was also performed using the uncoated spacer for SA fouling. In this case, the FRR was 69 %, which shows an enhancement in FRR with the coated spacer over the uncoated spacer for hydrogen peroxide mediated membrane cleaning.

Likewise, the cleaning of membrane fouled by HA deposition was also studied. A steep initial drop in flux was noted, which gradually stabilized over 2 h of crossflow filtration. The overall decline in flux over the HA filtration process was ~42 % (Fig. 8b). In this case, after photocatalytic cleaning, $PWP_{cleaned}$ was ~15 % higher than PWP_{fouled}, R_f was reduced by 28 % and the FRR was 60 %. Finally, the coated spacer was tested in cleaning the membrane after the filtration of BSA feed solution (Fig. 8c). Here, the flux was reduced by 48 % over the duration of the filtration stage. After photocatalytic cleaning, the R_f value decreased by 22 % and the an FRR of 54 % was achieved. In all three tests, the role of the spacer's photocatalytic activity in membrane cleaning was evident. The generation of electron-hole pairs in the feed helps in oxidizing the organic foulant species, and generating further reactive radicals. This is due to the decomposition of polysaccharide chains and carboxylic groups in the foulants to prevent further cross-linking [64].

3.5. Cyclic photocatalytic test

The cyclic tests were conducted with the modified membrane cell (see Figure S11, SI) for the increased light transmittance. The irradiance behind this modified cell was 4.36×103 μmol/m^{2}s in the 400–700 nm wavelength range, and 5.47 W/m^2 in the range of wavelength 315–400 nm. This additional transmittance of light could impact the performance of the coated materials, which is observed in the degradation of 10 ppm solution of MB as well in the dynamic filtration mode (Figure S12, SI). The FRR for cycle 1 with HA has risen to 81 %, compared to the 60 % for HA with the regular membrane cell. For cycle 2 and cycle 3, the FRR is 72 % and 71 % respectively. The drop is FRR from 81 % to 72 % between cycle 1 and cycle 2 can be attributed to the occurrence of irreversible membrane fouling by internal pore blockage after the first cycle [62]. For cycle 4, the FRR drops to 62 %. Here, we can observe that the effect of the photocatalytic spacer has decreased. The trend for the fouling resistance follows a similar pattern.

Next we observed the SEM images of the pristine and fouled membrane after the cyclic test (Fig. 10 c and d). It is observed that while there is clear membrane fouling after the tests, the integrity of the cylindrical
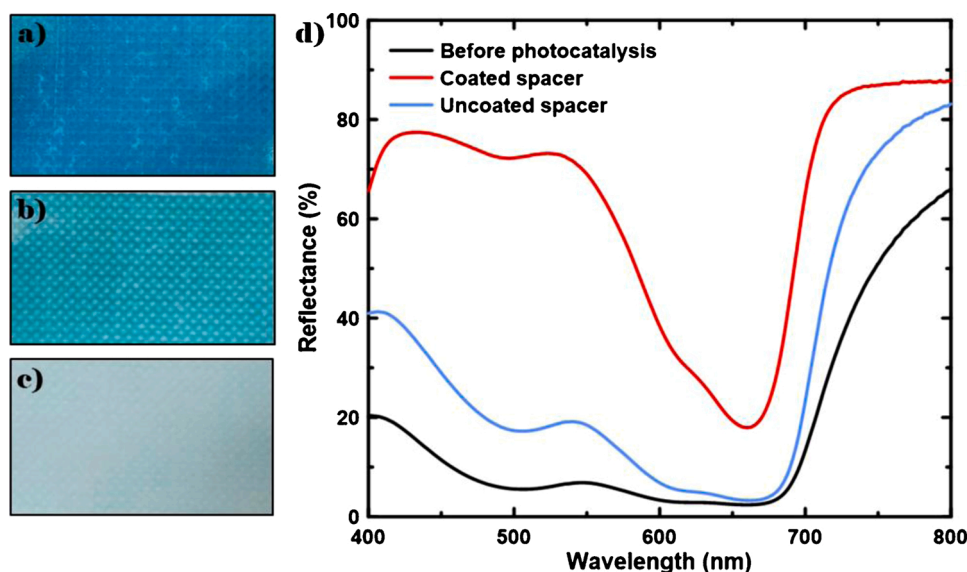

Fig. 7. Surface digital images of the membrane used in a 10 ppm MB filtration photocatalysis test: a) at the start of the photocatalysis, b) after photocatalysis in the absence of a coated spacer, c) after photocatalysis in the presence of coated spacer, showing a clear difference in membrane discoloration. D) diffuse-reflectance spectra of the membranes imaged in (a,b,c) to qualtitatively assess the rate of MB absorption on the membrane surface, using uncoated and coated spacers.
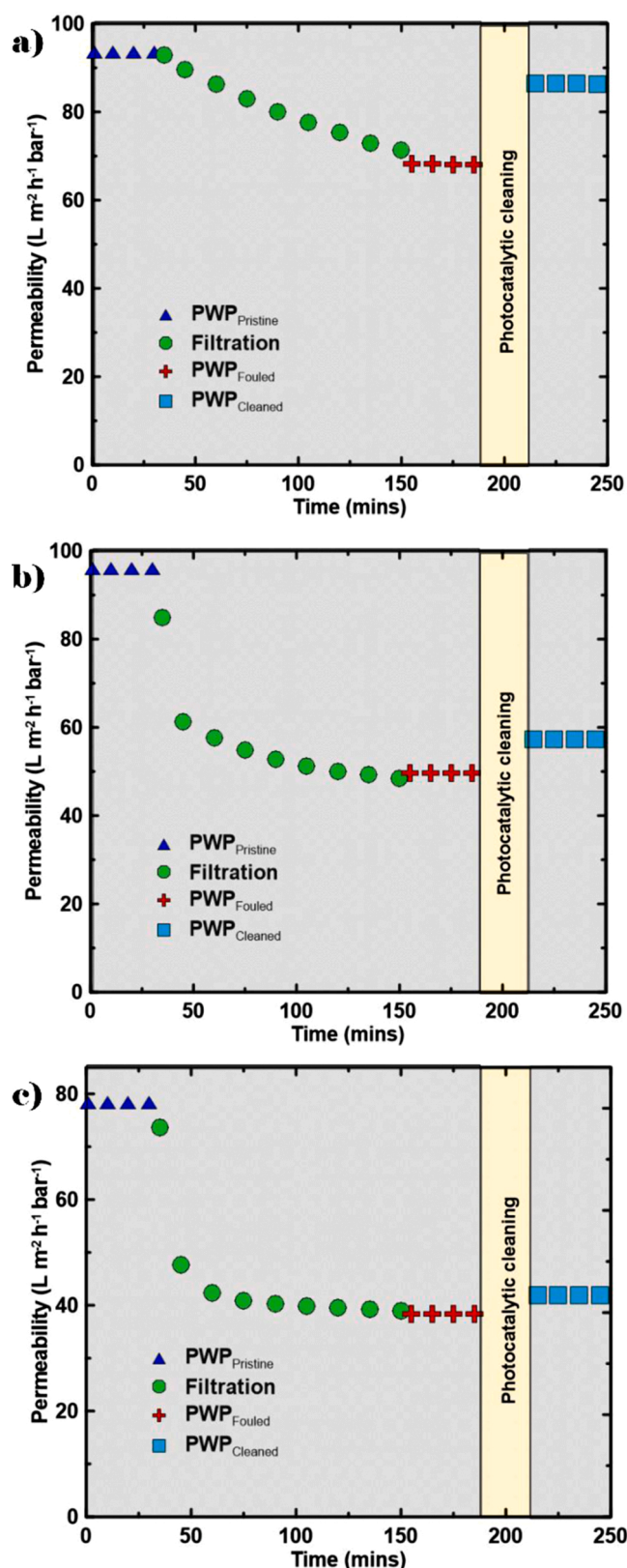
radical generation in this system, and also shields the membrane from direct irradiation by the UV light from the light source.

Finally, the performance of β−FeOOH coated spacer needs to be benchmarked. Since this is the first attempt to develop photocatalytic spacers with no precedent to compare to, the performance was benchmarked against that of state-of-the art photocatalytic membranes, which were developed to serve similar purposes. There are two key objectives of using photocatalytic membranes reported in literature: photocatalytic degradation of organic pollutant compounds in the feed or enabling membrane self-cleaning by photocatalytic activation. Both these objectives were fulfilled using our photocatalytic spacer. Therefore, two comparison tables were generated, Tables 3 and 4. In Table 3, the performance of β−FeOOH coated spacer was compared to photocatalytic membranes utilized to degrade organic pollutants in the feed (presented as pollutant removal, %), whereas in Table 4, the performance was compared to photocatalytic membranes used to mitigate fouling and enable membrane self-cleaning (quantified as FRR, %).

It can be seen that both the pollutant removal and self-cleaning efficiency of coated feed spacers was comparable, or superior in some cases, to those of state-of-the-art photocatalytic membranes. It is important to note that there are numerous other factors that influence the performance in a photocatalytic study, such as feed volume, operation mode (dead-end or crossflow; recirculation or single pass), intensity of light source, thickness of feed module, size of coated membrane, etc. However, the comparisons in Tables 3 and 4 confirm that feed spacers can indeed make for an efficient substitute for the membrane as a platform for photocatalyst immobilization. This approach has many advantages, as it allows the avoidance of most hurdles facing the development and implementation of photocatalytic membranes.

Some of the key challenges facing the wide adoption of photocatalytic membranes include reduced available photocatalyst surface area upon its impregnation into the membrane's polymer matrix, membrane damage from free radical generation on or within polymer matrix of the membrane, membrane ageing due to exposure to UV light and compromises to the membrane's permeability and/or selectivity after catalyst immobilization [65]. Since catalysis is related to surface adsorption [66,67], the location of the catalyst immobilization will typically be more vulnerable to damage from oxidation. Damage to a membrane through radicals or UV illumination can quickly lead to a negative effect on pore integrity, subsequently affecting the flux and reducing the rejection [68]. Shifting the focus of photocatalyst immobilization from the membrane to the spacer can allow the tackling of some of these issues effectively. Moreover, spacers can be made from a wide range of materials that can be more thermally and chemically stable than polymeric membranes. While ceramic and metallic membranes have been garnering attention for their potential use in catalyst immobilization [69–71], spacers can offer a cheaper and far more flexible alternative. 3D printing also allows the development of new spacers from metals [72] and ceramics [73], which can make extremely robust targets for catalyst immobilization. These materials can be much more resilient than membranes when it comes to chemical damage from radicals, and ensure that the water quality does not get affected.

By selecting spacers with high surface area per unit volume, such as the TPMS spacers herein used, the surface area of the immobilized catalyst can be maximized, with the potential of loading higher catalyst mass on the spacer than on the membrane. The use of photocatalytic spacers will also benefit the membrane by reducing the latter' interaction with the UV light and the generation of free radicals on or within membrane, which can lead to accelerated degradation of the membrane polymer chains. Additionally, spacer modification allows for more agility than membrane modification, with compromises to the membrane's rejection and selectivity not being a concern in the former route.

Another advantage of photocatalytic spacers is the potential utilization of H_2O_2 over NaOCl as a cleaning agent in membrane systems. NaOCl is a widely used cleaning agent, but it leads to the formation of

Fig. 8. Pure water permeability measurement before filtration, after filtration and after photocatalytic cleaning of 10 ppm solution of a) SA; b) HA; c) BSA.

pores remains intact. Similarly, the rejection of HA through the 4 cycles remains above 95 %. This is evidence of the membrane stability through the 4 cycles. In spite of repeated cycles of irradiation with solar light, the membrane is not damaged. The photocatalytic spacer is the source of
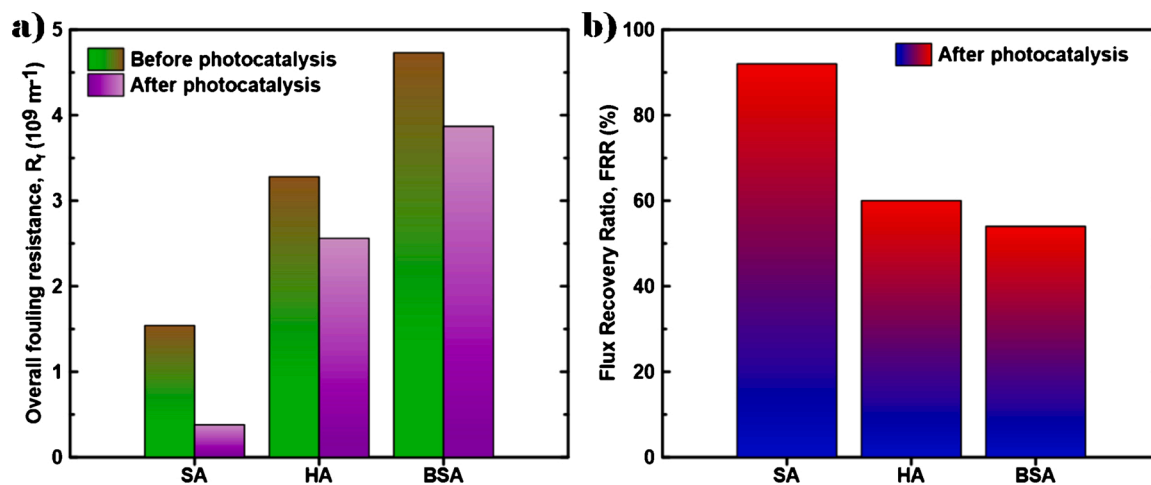
Fig. 9. a) Overall fouling resistance (R_f) after the filtration of SA, HA and BSA solution and before and after photocatalytic cleaning; b) flux recovery ratio (FRR, %) calculated after photocatalytic cleaning.
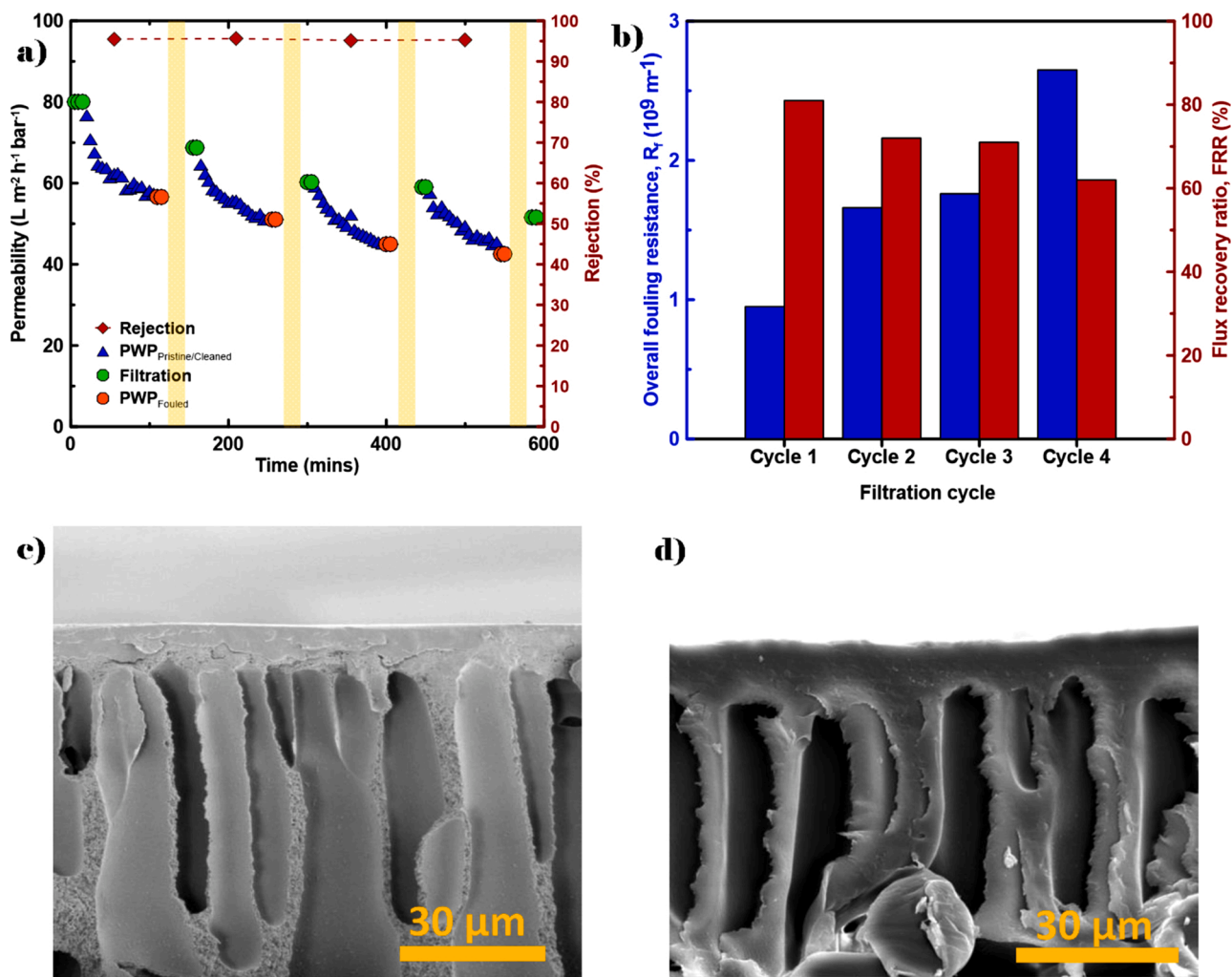

Fig. 10. a) Pure water permeability before filtration, after filtration and after photocatalytic cleaning of 10 ppm solution of HA for 4 continuous cycles; b) Overall fouling resistance (Rf) and flux recovery ratio (FRR, %) calculated after each cycle; cross-sectional SEM images of c) pristine membrane and d) used membrane after 4 cycles.

hazardous by-products and, thus, H_2O_2 has been promoted as a greener alternative [74]. However, the efficiency of H_2O_2 cleaning still leaves much to be desired, as it requires strongly alkaline conditions for its

performance to be comparable to NaOCl [74]. By coupling hydrogen peroxide cleaning with photocatalytic spacers, the cleaning effectiveness of the peroxide can be enhanced, making it a viable substitute for

Table 3

Performance of β-FeOOH coated spacer compared to photocatalytic membranes utilized to remove organic pollutants in the feed in eight photocatalytic membrane reactor studies.

Photocatalyst used	Pollutant	Conc.(ppm)	Light source	Pollutant removal (%)	Light duration (h)	Refs.
PVDF – $ZnIn_2S_4$	Fluvastatin	10	Sunlight	97	3*	[75]
g-C_3N_4 CT-rGO	Rhodamine B	5	Visible light	98	5*	[76]
PdTFPP-PVDF	MB	1	Green light	60	90*	[61]
Au-TiO_2/pDA/PVDF	Tetracycline	10	Visible light	92	2*	[77]
TiO_2-GO	MB	–	UV/Visible	90/100	1.5*	[78]
PVDF/(TiO_2/MWCNTs)	MB	10	UV	90	3*	[79]
β-FeOOH/PAN	MB	20	Visible	100	6*	[22]
g-C_3N_4 /TNA	Rhodamine B	3	Visible	60	3*	[80]
g-C_3N_4 NS/RGO/CA	Rhodamine B	5	Visible	60	1.5*	[8]
β-FeOOH	MB	25	Sunlight	98	4*	**This work**
β-FeOOH	4-NP	25	Sunlight	98	4*	**This work**

* Continuous irradiation.

Table 4

Performance of β-FeOOH coated spacer compared to photocatalytic membranes utilized to mitigate fouling and enable membrane self-cleaning.

Photocatalyst used	Pollutant	Conc.(ppm)	Light source	FRR (%)	Light duration (h)	Refs.
PES/TiO_2@Ni	SA	1000	UV/Sunlight	92/77	6/1**	[62]
PES/TiO_2@Ni	BSA	1000	UV/Sunlight	75/41	6/1**	[62]
PES/TiO_2@Ni	HA	1000	UV/Sunlight	98/78	6/1**	[62]
PVDF/TiO_2-ZnO	HA	20	Visible light	70	1*	[81]
PVDF_LiCl-TiO_2	HA	2	UV	52	1.6*	[82]
PVDF – $ZnIn_2S_4$	Rhodamine B	15	Sunlight	80	3*	[75]
TNTs/PES-F-COOH	Polyacrylamide	1000	Sunlight	80	0.33**	[83]
β-FeOOH/PAN	MB	20	Visible	96	0.5**	[22]
β-FeOOH	SA	10	Sunlight	92	0.5**	**This work**
β-FeOOH	HA	10	Sunlight	60	0.5**	**This work**
β-FeOOH	BSA	10	Sunlight	54	0.5**	**This work**

* Continuous irradiation.
** Intermittent irradiation.

NaOCl as a cleaning agent.

A significant challenge that is facing the adoption of photocatalytic membrane reactors is the design of membrane modules that enable the illumination of the photocatalyst layer with the light source. This is equally relevant to photocatalytic spacers as it is to membranes. A direct and immediate application of the current photocatalytic spacer design would be for a simple plate and frame module design. However, the adaptability of the photocatalytic process for SWMs will need systematic research on engineering the SWM to be suitable as a photocatalytic membrane reactor. Some of the scenarios that can be investigated in the future include: i) varying the material of module housing and seal for better light penetration and ii) exploring the possibilities of introducing light to the SWM at additional points such as via the central permeate collection tube and over the module seals. Considering the transmission loss through each wound membrane layer one can also study the effect of increasing source light intensity on the process efficiency. Alternatively, one could also consider sectioned and shorter SWM arrangement interjected axially with light sources. These solutions would need to be supplemented with a cost benefit analysis to compare the increased cost of light intensity and the benefit of photocatalytic degradation. In the upcoming years, the design of internally illuminated membrane modules will remain a gaping hole that needs to be addressed to make photocatalytic membrane reactors both practical and feasible.

4. Conclusion

In this study, we developed novel β−FeOOH nanorods-coated 3D printed feed spacers to be utilized in the simultaneous photocatalytic degradation of membrane-permeating hazardous organic pollutants during membrane filtration processes in water treatment applications. Such pollutants are not typically rejected by ultrafiltration membranes and require additional downstream treatment for their degradation and removal. A 3D printed feed spacer based on the TPMS architecture was modified through PDA/PEI mediated coating of β−FeOOH nanorods in a two-step process. The β−FeOOH nanorods coating acted as a photocatalyst in the presence of solar light and H_2O_2 in the feed solution. The formation of β−FeOOH nanorods and their attachment to the spacer were confirmed using XRD, ATR-FTIR, SEM and EDX data. The impacts of the nanorods on the spacer's surface micro-roughness and hydrophilicity were also established. The efficacy of the coated spacers in the photocatalytic degradation of MB and 4-NP pollutants in the feed solution was verified in both batch and dynamic crossflow filtration modes, and at two concentrations (10 and 25 ppm). The modified spacer has proven to be highly efficient for photocatalytic degradation of pollutants in batch mode, although its efficiency was partially reduced during the dynamic filtration mode, due to the partial hindrance created by the acrylic filtration cell for the passage of UV light. Even with this hindrance, the spacer was capable of achieving a remarkable 98 % removal of both chemicals during a 4 h filtration test.

Another important new feature of the photocatalytic spacer is its ability to clean the membrane. This feature was studied by evaluating the ability of the photocatalytic spacer to recover the membrane flux, after it was reduced by cake-forming solutes such as SA, HA and BSA. In each case, the coated spacer was capable of recovering lost flux through the removal of the foulant deposited on the membrane surface. The FRR and R_f of the membrane were calculated to quantify this recovery. The coated feed spacer achieved FRR ranging from 54 to 92% for the three foulants, while the fouling resistance, R_f, was evidently much lower after cleaning by photocatalysis. The values obtained using β−FeOOH coated spacer of two performance parameters (pollutant removal (%) and FRR) were on par or even better than those reported in literature for photocatalytic membranes. Hence, β−FeOOH coated spacers can provide an interesting and practical venue to address some of the challenges of photocatalytic membrane reactors and their applicability in water treatment.

CRediT authorship contribution statement

Nurshaun Sreedhar: Conceptualization, Methodology, Data curation, Formal analysis, Investigation, Validation, Visualization, Writing - original draft. **Mahendra Kumar:** Methodology, Validation, Data curation. **Samar Al Jitan:** Data curation, Investigation, Formal analysis. **Navya Thomas:** Visualization, Writing - review & editing. **Giovanni Palmisano:** Supervision, Resources, Writing - review & editing. **Hassan A. Arafat:** Conceptualization, Methodology, Project administration, Supervision, Funding acquisition.

Declaration of Competing Interest

The authors report no declarations of interest.

Acknowledgments

Appendix A. Supplementary data

Supplementary material related to this article can be found, in the online version, at doi:https://doi.org/10.1016/j.apcatb.2021.120318.

References

[1] Y. Shi, J. Huang, G. Zeng, W. Cheng, J. Hu, Photocatalytic membrane in water purification: is it stepping closer to be driven by visible light? J. Memb. Sci. 584 (2019) 364–392.

[2] G. Boczkaj, A. Fernandes, Wastewater treatment by means of advanced oxidation processes at basic pH conditions: a review, Chem. Eng. J. 320 (2017) 608–633.

[3] D. Kanakaraju, B.D. Glass, M. Oelgemöller, Advanced oxidation process-mediated removal of pharmaceuticals from water: a review, J. Environ. Manage. 219 (2018) 189–207.

[4] D. Toledano Garcia, L.Y. Ozer, F. Parrino, M. Ahmed, G.P. Brudecki, S.W. Hasan, G. Palmisano, Photocatalytic ozonation under visible light for the remediation of water effluents and its integration with an electro-membrane bioreactor, Chemosphere. 209 (2018) 534–541.

[5] W. Zhang, L. Ding, J. Luo, M.Y. Jaffrin, B. Tang, Membrane fouling in photocatalytic membrane reactors (PMRs) for water and wastewater treatment: a critical review, Chem. Eng. J. 302 (2016) 446–458.

[6] R. Molinari, C. Lavorato, P. Argurio, Recent progress of photocatalytic membrane reactors in water treatment and in synthesis of organic compounds, A review, Catal. Today. 281 (2017) 144–164.

[7] L. Paredes, S. Murgolo, H. Dzinun, M.H. Dzarfan Othman, A.F. Ismail, M. Carballa, G. Mascolo, Application of immobilized TiO2 on PVDF dual layer hollow fibre membrane to improve the photocatalytic removal of pharmaceuticals in different water matrices, Appl. Catal. B Environ. 240 (2019) 9–18.

[8] H. Zhao, S. Chen, X. Quan, H. Yu, H. Zhao, Integration of microfiltration and visible-light-driven photocatalysis on g-C3N4 nanosheet/reduced graphene oxide membrane for enhanced water treatment, Appl. Catal. B Environ. 194 (2016) 134–140.

[9] X. Zheng, Z.-P. Shen, L. Shi, R. Cheng, D.-H. Yuan, Photocatalytic membrane reactors (PMRs) in water treatment: configurations and influencing factors, Catalysts 7 (2017) 224.

[10] R. Goei, T.T. Lim, Ag-decorated TiO2 photocatalytic membrane with hierarchical architecture: photocatalytic and anti-bacterial activities, Water Res. 59 (2014) 207–218.

[11] Y. Gao, M. Hu, B. Mi, Membrane surface modification with TiO2-graphene oxide for enhanced photocatalytic performance, J. Memb. Sci. 455 (2014) 349–356.

[12] S. Yu, Y. Wang, F. Sun, R. Wang, Y. Zhou, Novel mpg-C3N4/TiO2 nanocomposite photocatalytic membrane reactor for sulfamethoxazole photodegradation, Chem. Eng. J. 337 (2018) 183–192.

[13] G. Liu, K. Han, H. Ye, C. Zhu, Y. Gao, Y. Liu, Y. Zhou, Graphene oxide/triethanolamine modified titanate nanowires as photocatalytic membrane for water treatment, Chem. Eng. J. 320 (2017) 74–80.

[14] A. Lee, J.A. Libera, R.Z. Waldman, A. Ahmed, J.R. Avila, J.W. Elam, S.B. Darling, Conformal nitrogen-doped TiO 2 photocatalytic coatings for sunlight-activated membranes, Adv. Sustain. Syst. 1 (2017), 1600041.

[15] H. Zhang, A.U. Mane, X. Yang, Z. Xia, E.F. Barry, J. Luo, Y. Wan, J.W. Elam, S. B. Darling, Visible-light-Activated photocatalytic films toward self-cleaning membranes, Adv. Funct. Mater. 30 (2020) 1–9.

[16] Y. AlSalka, L.I. Granone, W. Ramadan, A. Hakki, R. Dillert, D.W. Bahnemann, Iron-based photocatalytic and photoelectrocatalytic nano-structures: facts, perspectives, and expectations, Appl. Catal. B Environ. 244 (2019) 1065–1095.

[17] A.R. Amani-Ghadim, S. Alizadeh, F. Khodam, Z. Rezvani, Synthesis of rod-like α-FeOOH nanoparticles and its photocatalytic activity in degradation of an azo dye: Empirical kinetic model development, J. Mol. Catal. A Chem. 408 (2015) 60–68.

[18] T. Zhu, W.L. Ong, L. Zhu, G.W. Ho, TiO2 fibers supported β-FeOOH nanostructures as efficient visible light photocatalyst and room temperature gas sensor, Sci. Rep. 5 (2015) 1–15.

[19] Y. Zheng, Z. Zhang, C. Li, Beta-FeOOH-supported graphitic carbon nitride as an efficient visible light photocatalyst, J. Mol. Catal. A Chem. 423 (2016) 463–471.

[20] X. Qian, Y. Wu, M. Kan, M. Fang, D. Yue, J. Zeng, Y. Zhao, FeOOH quantum dots coupled g-C3N4 for visible light driving photo- Fenton degradation of organic pollutants, Appl. Catal. B Environ. 237 (2018) 513–520.

[21] Z. Wang, H.C. Yang, F. He, S. Peng, Y. Li, L. Shao, S.B. Darling, Mussel-inspired surface engineering for water-remediation materials, Matter. 1 (2019) 115–155.

[22] Y. Lv, C. Zhang, A. He, S.J. Yang, G.P. Wu, S.B. Darling, Z.K. Xu, Photocatalytic nanofiltration membranes with self-cleaning property for wastewater treatment, Adv. Funct. Mater. 27 (2017) 1–8.

[23] J. Chen, X. Meng, Y. Tian, X. Wang, J. Zhu, H. Zheng, L. Wang, Fabrication of a superhydrophilic PVDF-g-PAA@FeOOH ultrafiltration membrane with visible light photo-fenton self-cleaning performance, J. Memb. Sci. 616 (2020), 118587.

[24] J. Schwinge, P.R. Neal, D.E. Wiley, D.F. Fletcher, A.G. Fane, Spiral wound modules and spacers: review and analysis, J. Memb. Sci. 242 (2004) 129–153.

[25] H.S. Abid, D.J. Johnson, R. Hashaikeh, N. Hilal, A review of efforts to reduce membrane fouling by control of feed spacer characteristics, Desalination 420 (2017) 0–1.

[26] D.J. Miller, P.A. Araújo, P.B. Correia, M.M. Ramsey, J.C. Kruithof, M.C.M. van Loosdrecht, B.D. Freeman, D.R. Paul, M. Whiteley, J.S. Vrouwenvelder, Short-term adhesion and long-term biofouling testing of polydopamine and poly(ethylene glycol) surface modifications of membranes and feed spacers for biofouling control, Water Res. 46 (2012) 3737–3753.

[27] R. Hausman, T. Gullinkala, I.C. Escobar, Development of copper-charged polypropylene feedspacers for biofouling control, J. Memb. Sci. 358 (2010) 114–121.

[28] K. Reid, M. Dixon, C. Pelekani, K. Jarvis, M. Willis, Y. Yu, Biofouling control by hydrophilic surface modification of polypropylene feed spacers by plasma polymerisation, Desalination. 335 (2014) 108–118.

[29] A. Ronen, S. Lerman, G.Z. Ramon, C.G. Dosoretz, Experimental characterization and numerical simulation of the anti-biofuling activity of nanosilver-modified feed spacers in membrane filtration, J. Memb. Sci. 475 (2015) 320–329.

[30] A. Ronen, R. Semiat, C.G. Dosoretz, Impact of ZnO embedded feed spacer on biofilm development in membrane systems, Water Res. 47 (2013) 6628–6638.

[31] T. Vercellino, P. Tran, T. Reid, A. Hamood, A. Morse, Evaluation of polymerized organo-selenium feed spacers to inhibit S. Aureus and E. Coli biofilm development in reverse osmosis systems, Desalination. 331 (2013) 1–5.

[32] T. Vercellino, A. Morse, P. Tran, A. Hamood, T. Reid, L. Song, T. Moseley, The use of covalently attached organo-selenium to inhibit S. Aureus and E. Coli biofilms on {RO} membranes and feed spacers, Desalination. 317 (2013) 142–151.

[33] W. Yang, M. Son, B. Xiong, M. Kumar, S. Bucs, J.S. Vrouwenvelder, B.E. Logan, Effective biofouling control using periodic H 2 O 2 cleaning with CuO modified and polypropylene spacers, ACS Sustain. Chem. Eng. (2019) acssuschemeng.9b01086.

[34] N. Sreedhar, N. Thomas, O. Al-Ketan, R. Rowshan, H. Hernandez, R.K. Abu Al-Rub, H.A. Arafat, 3D printed feed spacers based on triply periodic minimal surfaces for flux enhancement and biofouling mitigation in RO and UF, Desalination. 425 (2018) 12–21.

[35] N. Sreedhar, N. Thomas, O. Al-Ketan, R. Rowshan, H.H. Hernandez, R.K. Abu Al-Rub, H.A. Arafat, Mass transfer analysis of ultrafiltration using spacers based on triply periodic minimal surfaces: effects of spacer design, directionality and voidage, J. Memb. Sci. 561 (2018) 89–98.

[36] N. Thomas, N. Sreedhar, O. Al-Ketan, R. Rowshan, R.K. Abu Al-Rub, H. Arafat, 3D printed triply periodic minimal surfaces as spacers for enhanced heat and mass transfer in membrane distillation, Desalination 443 (2018) 256–271.

[37] M. Zhang, H. Lin, L. Shen, B.Q. Liao, X. Wu, R. Li, Effect of calcium ions on fouling properties of alginate solution and its mechanisms, J. Memb. Sci. 525 (2017) 320–329.

[38] K. Listiarini, L. Tan, D.D. Sun, J.O. Leckie, Systematic study on calcium-alginate interaction in a hybrid coagulation-nanofiltration system, J. Memb. Sci. 370 (2011) 109–115.

[39] N. Sreedhar, N. Thomas, O. Al-Ketan, R. Rowshan, R.K. Abu Al-Rub, S. Hong, H. A. Arafat, Impacts of feed spacer design on UF membrane cleaning efficiency, J. Memb. Sci. 616 (2020), 118571.

[40] Y. Lv, Y. Du, Z.X. Chen, W.Z. Qiu, Z.K. Xu, Nanocomposite membranes of polydopamine/electropositive nanoparticles/polyethyleneimine for nanofiltration, J. Memb. Sci. 545 (2018) 99–106.

[41] C. Eswaraiah, R. Sakthivel, D. Behera, B.K. Mishra, Synthesis and characterization of nanomaterials derived from mineral waste, Nanosci. Nanotechnol. Lett. 3 (2011) 166–169.

[42] R. Chen, I.K. Puri, I. Zhitomirsky, High areal capacitance of FeOOH-carbon nanotube negative electrodes for asymmetric supercapacitors, Ceram. Int. 44 (2018) 18007–18015.

[43] J. Fan, Z. Zhao, Z. Ding, J. Liu, Synthesis of different crystallographic FeOOH catalysts for peroxymonosulfate activation towards organic matter degradation, RSC Adv. 8 (2018) 7269–7279.

[44] Q. Wang, A. Puntambekar, V. Chakrapani, Gaseous reactions in adsorbed water present on transition metal oxides, J. Phys. Chem. C. 121 (2017) 13151–13163.

[45] S. Xiong, Y. Wang, J. Yu, L. Chen, J. Zhu, Z. Hu, Polydopamine for next-generation multifunctional biocomposites, J. Mater. Chem. A Mater. Energy Sustain. 2 (2014) 7578–7587.

[46] D. Garcia, G. Picasso, P. Hidalgo, H.E.M. Peres, R. Sun Kou, J.M. Gonçalves, Sensors based on Ag-loaded hematite (α-Fe2O3) nanoparticles for methyl mercaptan detection at room temperature, Anal. Chem. Res. 12 (2017) 74–81.

[47] K. Zarrini, M. Youssefi, An investigation into the structure and morphology of polyamide 6/polyaniline hybrid fibers, J. Polym. Eng. 38 (2018) 19–24.

[48] S. Zhou, Q. Zhang, J. Huang, D. Ding, Friction and wear behaviors of polyamide-based composites blended with polyphenylene sulfide, J. Thermoplast. Compos. Mater. 27 (2014) 977–991.

[49] J. Jung, K. Song, D.R. Bae, S.W. Lee, G. Lee, Y.M. Kang, β-FeOOH nanorod bundles with highly enhanced round-trip efficiency and extremely low overpotential for lithium-air batteries, Nanoscale. 5 (2013) 11845–11849.

[50] J.C. Farias-Aguilar, M.J. Ramírez-Moreno, L. Téllez-Jurado, H. Balmori-Ramírez, Low pressure and low temperature synthesis of polyamide-6 (PA6) using Na0 as catalyst, Mater. Lett. 136 (2014) 388–392.

[51] K. Liu, Y. Li, L. Tao, R. Xiao, Preparation and characterization of polyamide 6 fibre based on a phosphorus-containing flame retardant, RSC Adv. 8 (2018) 9261–9271.

[52] K. Shrimali, J. Jin, B.V. Hassas, X. Wang, J.D. Miller, The surface state of hematite and its wetting characteristics, J. Colloid Interface Sci. 477 (2016) 16–24.

[53] Y. Huang, Y. Gao, Q. Zhang, Y. Zhang, Y. ji Cao, W. Ho, S.C. Lee, Biocompatible FeOOH-Carbon quantum dots nanocomposites for gaseous NOx removal under visible light: improved charge separation and High selectivity, J. Hazard. Mater. 354 (2018) 54–62.

[54] X. Wang, W. Lu, Z. Zhao, H. Zhong, Z. Zhu, W. Chen, In situ stable growth of β-FeOOH on g-C3N4 for deep oxidation of emerging contaminants by photocatalytic activation of peroxymonosulfate under solar irradiation, Chem. Eng. J. 400 (2020) 125872.

[55] L. Zhou, S. Yan, B. Tian, J. Zhang, M. Anpo, Preparation of TiO2-SiO2 film with high photocatalytic activity on PET substrate, Mater. Lett. 60 (2006) 396–399.

[56] K. Zhang, Y. Liu, J. Deng, S. Xie, H. Lin, X. Zhao, J. Yang, Z. Han, H. Dai, Fe2O3/3DOM BiVO4: High-performance photocatalysts for the visible light-driven degradation of 4-nitrophenol, Appl. Catal. B Environ. 202 (2017) 569–579.

[57] B. Yuan, X. Li, K. Li, W. Chen, Degradation of dimethyl phthalate (DMP) in aqueous solution by UV/Si-FeOOH/H2O2, Colloids Surfaces A Physicochem, Int. J. Pavement Eng. Asph. Technol. 379 (2011) 157–162.

[58] J.P. Méricq, J. Mendret, S. Brosillon, C. Faur, High performance PVDF-TiO2 membranes for water treatment, Chem. Eng. Sci. 123 (2015) 283–291.

[59] L. Zhang, T.C.A. Ng, X. Liu, Q. Gu, Y. Pang, Z. Zhang, Z. Lyu, Z. He, H.Y. Ng, J. Wang, Hydrogenated TiO2 membrane with photocatalytically enhanced anti-fouling for ultrafiltration of surface water, Appl. Catal. B Environ. 264 (2020), 118528.

[60] X.D. Du, X.H. Yi, P. Wang, W. Zheng, J. Deng, C.C. Wang, Robust photocatalytic reduction of Cr(VI) on UiO-66-NH2(Zr/Hf) metal-organic framework membrane under sunlight irradiation, Chem. Eng. J. 356 (2019) 393–399.

[61] R. Lyubimenko, D. Busko, B.S. Richards, A.I. Schäfer, A. Turshatov, Efficient photocatalytic removal of methylene blue using a metalloporphyrin-poly (vinylidene fluoride) hybrid membrane in a flow-through reactor, ACS Appl. Mater. Interfaces 11 (2019) 31763–31776.

[62] T. Sun, Y. Liu, L. Shen, Y. Xu, R. Li, L. Huang, H. Lin, Magnetic field assisted arrangement of photocatalytic TiO2 particles on membrane surface to enhance membrane antifouling performance for water treatment, J. Colloid Interface Sci. 570 (2020) 273–285.

[63] R. Kumar, A.F. Ismail, Fouling control on microfiltration/ultrafiltration membranes: effects of morphology, hydrophilicity, and charge, J. Appl. Polym. Sci. 132 (2015) n/a-n/a.

[64] L.T. Nyamutswa, B. Zhu, S.F. Collins, D. Navaratna, M.C. Duke, Light conducting photocatalytic membrane for chemical-free fouling control in water treatment, J. Memb. Sci. 604 (2020), 118018.

[65] M. Romay, N. Diban, M.J. Rivero, A. Urtiaga, I. Ortiz, Critical issues and guidelines to improve the performance of photocatalytic polymeric membranes, Catalysts 10 (2020) 570.

[66] N. Serpone, A.V. Emeline, Modelling heterogeneous photocatalysis by metal-oxide nanostructured semiconductor and insulator materials: factors that affect the activity and selectivity of photocatalysts, Res. Chem. Intermed. 31 (2005) 391–432.

[67] A. Turolla, A. Piazzoli, J. Farner Budarz, M.R. Wiesner, M. Antonelli, Experimental measurement and modelling of reactive species generation in TiO2 nanoparticle photocatalysis, Chem. Eng. J. 271 (2015) 260–268.

[68] W. Fu, W. Zhang, Chemical aging and impacts on hydrophilic and hydrophobic polyether sulfone (PES) membrane filtration performances, Polym. Degrad. Stab. 168 (2019), 108960.

[69] J.W. Maina, J.A. Schütz, L. Grundy, E. Des Ligneris, Z. Yi, L. Kong, C. Pozo-Gonzalo, M. Ionescu, L.F. Dumée, Inorganic Nanoparticles/Metal organic framework hybrid membrane reactors for efficient photocatalytic conversion of CO2, ACS Appl. Mater. Interfaces 9 (2017) 35010–35017.

[70] S. Wang, J. Tian, Q. Wang, F. Xiao, S. Gao, W. Shi, F. Cui, Development of CuO coated ceramic hollow fiber membrane for peroxymonosulfate activation: a highly efficient singlet oxygen-dominated oxidation process for bisphenol a degradation, Appl. Catal. B Environ. 256 (2019), 117783.

[71] Y. Bao, W.J. Lee, T.T. Lim, R. Wang, X. Hu, Pore-functionalized ceramic membrane with isotropically impregnated cobalt oxide for sulfamethoxazole degradation and membrane fouling elimination: synergistic effect between catalytic oxidation and membrane separation, Appl. Catal. B Environ. 254 (2019) 37–46.

[72] C. Buchanan, L. Gardner, Metal 3D printing in construction: a review of methods, research, applications, opportunities and challenges, Eng. Struct. 180 (2019) 332–348.

[73] X. Liu, B. Zou, H. Xing, C. Huang, The preparation of ZrO2-Al2O3 composite ceramic by SLA-3D printing and sintering processing, Ceram. Int. 46 (2020) 937–944.

[74] K. Li, S. Li, T. Huang, C. Dong, J. Li, B. Zhao, S. Zhang, Chemical cleaning of ultrafiltration membrane fouled by humic substances: comparison between hydrogen peroxide and sodium hypochlorite, Int. J. Environ. Res. Public Health 16 (2019) 2568.

[75] T. Liu, L. Wang, X. Liu, C. Sun, Y. Lv, R. Miao, X. Wang, Dynamic photocatalytic membrane coated with ZnIn2S4 for enhanced photocatalytic performance and antifouling property, Chem. Eng. J. 379 (2020), 122379.

[76] Y. Wei, Y. Zhu, Y. Jiang, Photocatalytic self-cleaning carbon nitride nanotube intercalated reduced graphene oxide membranes for enhanced water purification, Chem. Eng. J. 356 (2019) 915–925.

[77] C. Wang, Y. Wu, J. Lu, J. Zhao, J. Cui, X. Wu, Y. Yan, P. Huo, Bioinspired synthesis of photocatalytic nanocomposite membranes based on synergy of Au-TiO2 and polydopamine for degradation of tetracycline under visible light, ACS appl. Mater. Interfaces. 9 (2017) 23687–23697.

[78] N.A. Almeida, P.M. Martins, S. Teixeira, J.A. Lopes da Silva, V. Sencadas, K. Kühn, G. Cuniberti, S. Lanceros-Mendez, P.A.A.P. Marques, TiO2/graphene oxide immobilized in P(VDF-TrFE) electrospun membranes with enhanced visible-light-induced photocatalytic activity, J. Mater. Sci. 51 (2016) 6974–6986.

[79] J. Cheng, H. Pu, A facile method to prepare polyvinylidene fluoride composite nanofibers with high photocatalytic activity via nanolayer coextrusion, Eur. Polym. J. 99 (2018) 361–367.

[80] Q. Zhang, X. Quan, H. Wang, S. Chen, Y. Su, Z. Li, Constructing a visible-light-driven photocatalytic membrane by g-C3N4 quantum dots and TiO2 nanotube array for enhanced water treatment, Sci. Rep. 7 (2017) 1–7.

[81] N. Li, Y. Tian, J. Zhang, Z. Sun, J. Zhao, J. Zhang, W. Zuo, Precisely-controlled modification of PVDF membranes with 3D TiO2/ZnO nanolayer: enhanced anti-fouling performance by changing hydrophilicity and photocatalysis under visible light irradiation, J. Memb. Sci. 528 (2017) 359–368.

[82] H. Song, J. Shao, J. Wang, X. Zhong, The removal of natural organic matter with LiCl-TiO2-doped PVDF membranes by integration of ultrafiltration with photocatalysis, Desalination. 344 (2014) 412–421.

[83] Z. Geng, X. Wang, H. Jiang, L. Zhang, Z. Chen, Y. Feng, W. Geng, X. Yang, M. Huo, J. Sun, High-Performance TiO2 Nanotubes/Poly(aryl ether sulfone) Hybrid Self-Cleaning Anti-Fouling Ultrafiltration Membranes, Polymers (Basel). 11 (2019) 555.